On the effect of the East/Japan Sea SST variability on the North Pacific atmospheric circulation in a regional climate model

Hyodae Seo[1], Young-Oh Kwon[1], and Jong-Jin Park[2]

[1]Woods Hole Oceanographic Institution, Woods Hole, Massachusetts, USA, [2]Department of Oceanography, Kyungpook National University, Sangju, South Korea

Abstract The East/Japan Sea (EJS) is a semi-enclosed marginal sea located in the upstream of the North Pacific storm track, where the leading modes of wintertime interannual variability in sea surface temperature (SST) are characterized by the basin-wide warming-cooling and the northeast-southwest dipole. Processes leading to local and remote atmospheric responses to these SST anomalies are investigated using the Weather Research and Forecast (WRF) model. The atmosphere in direct contact with anomalous diabatic forcing exhibits a linear and symmetric response with respect to the sign, pattern, and magnitude of SST anomalies, producing increased (decreased) wind speed and precipitation response over warm (cold) SSTs. This local response is due to modulation of both the vertical stability of the marine atmospheric boundary layer and the adjustment of sea level pressure, although the latter provides a better explanation of the quadrature relationship between SST and wind speed. The linearity in the local response suggests the importance of fine-scale EJS SSTs to predictability of the regional weather and climate variability. The remote circulation response, in contrast, is strongly nonlinear. An intraseasonal equivalent barotropic ridge emerges in the Gulf of Alaska as a common remote response independent of EJS SST anomalies. This downstream blocking response is reinforced by the enhanced storm track variability east of Japan via transient eddy vorticity flux convergence. Strong nonlinearity in remote response implies that detailed EJS SST patterns may not be critical to this downstream ridge response. Overall, results demonstrate a remarkably far-reaching impact of the EJS SSTs on the atmospheric circulation.

1. Introduction

Anomalies in the extratropical sea surface temperature (SST) are generated primarily as local and remote response to air-sea heat and momentum fluxes modulated by the near-surface atmospheric conditions [*Frankignoul and Hasselmann*, 1977; *Frankignoul and Reynolds*, 1983]. These extratropical SST anomalies, in turn, influence the middle- to high-latitude atmospheric circulation on seasonal to decadal timescales [*Frankignoul*, 1985; *Latif and Barnett*, 1994; *Kushnir et al.*, 2002; *Kwon et al.*, 2010]. Results from previous studies of linear baroclinic models and primitive equations atmospheric general circulation models (AGCMs) suggest two distinctive dynamical processes by which the extratropical SST anomalies influence the large-scale wintertime atmospheric circulation. As a direct response to anomalous diabatic heating, the initial response is thermally driven with a baroclinic vertical structure [*Hoskins and Karoly*, 1981; *Deser et al.*, 2007]. The response is confined to the vicinity of forcing, where the sign, structure, and amplitude of the response correspond to those of SST anomalies [e.g., *Palmer and Sun*, 1985; *Ferranti et al.*, 1994]. This linear initial response is transient in that it is rapidly (~2 weeks, e.g., *Deser et al.* [2007]) replaced with the nonlinear response with a much broader spatial extent and magnitude than the initial response [*Ferreira and Frankignoul*, 2005, 2008].

Driven by nonlocal dynamical effect of synoptic transient eddies [*Kushnir and Lau*, 1992; *Peng et al.*, 1995; *Peng and Whitaker*, 1999; *Peng and Robinson*, 2001; *Kushnir et al.*, 2002], the equilibrium response typically features an equivalent barotropic ridge in the downstream of the diabatic forcing, producing an antisymmetric response with respect to those of SST anomalies [*Pitcher et al.*, 1988; *Kushnir and Lau*, 1992; *Magnusdottir et al.*, 2004]. The effect of transient eddies depends on the storm track climatology of the model and the location of SST anomalies relative to this storm track [*Ting and Peng*, 1995; *Peng and Whitaker*, 1999], implying that the SST anomalies in the vicinity of the climatological storm track would effectively induce an equivalent barotropic high response via altere storm track activity [e.g., *Walter et al.*, 2001; *Peng and Robinson*,

2001]. Such a quasi-stationary circulation response projects onto the dominant modes of internal atmospheric variability [*Peng and Robinson*, 2001; *Deser et al.*, 2004, 2007; *Frankignoul and Sennéchael*, 2007], resembling the anomalous atmospheric circulation responsible for the SST anomalies to being with. This implies an extratopical coupled mode of variability [*Latif and Barnett*, 1994, 1996; *Kushnir et al.*, 2002; *Ferreira and Frankignoul*, 2005]. *Liu and Wu* [2004] reported that the strongest and the most realistic equivalent barotropic ridge response is found in a fully coupled GCM simulation in comparison to those that are only partially or not coupled. Previous studies suggested that the ocean-to-atmospheric feedback is most effective near the western boundary current region of each basin, where the storm track encounters intense air-sea heat flux variability due to changes in ocean advection [e.g., *Kelly et al.*, 2010; *Kwon et al.*, 2010].

In the northwest Pacific abutting the East Asian continental margins, there is a chain of smaller seas known as the East Asian Marginal Seas, which consist of the East China Sea, the Yellow Sea, the East/Japan Sea (hereafter referred to as the EJS), and the Okhotsk Sea. These marginal seas are influenced by the variability of the greater western boundary current system of the northwest Pacific Ocean [e.g., *Minato and Kimura*, 1980; *Hirose and Fukudome*, 2006]. Located upstream of the climatological storm track, the air-sea interactions in these marginal seas may be important for the downstream large-scale atmospheric circulation [*Hirose et al.*, 2009], a unique process in the northwest Pacific that is absent in the North Atlantic [*Kelly et al.*, 2010]. The EJS, the focus of this study, is a semi-enclosed marginal sea that is sandwiched between the cold continent influenced by the Siberian High and the warm maritime conditions of the western boundary current. The EJS is subject to strong influence under the seasonal monsoon system. During the winter season, defined as November through April (NDJFMA) in this study, the northwesterly advection of dry and cold continental air mass over the warm EJS facilitates an intense air mass modification process, leading to a substantial transfer of heat and moisture to the atmosphere, frequent formation of maritime clouds, and extreme precipitation events [*Manabe*, 1957; *Ninomiya*, 1964; *Na et al.*, 1999]. These processes tend to be prevalent during the period of cold air outbreaks [*Dorman et al.*, 2004; *Isobe and Beardsley*, 2007; *Takano et al.*, 2008].

The dominant modes of the low-frequency EJS SST variability are identified from the Empirical Orthogonal Function (EOF) analysis applied to the wintertime (NDJFMA) daily National Oceanic and Atmospheric Administration (NOAA) Optimum Interpolation (OI) ¼° SST analysis [*Reynolds et al.*, 2007] from 1982 through 2010. The first mode (Figure 1b), explaining 42% of the total variance, represents the basin-wide warming and cooling with peaks near the mean position of the climatological subpolar front (Figure 1a). The SST anomalies of >0.5°C near the subpolar front represent the changes in position and intensity of the front. The maximum positive SST anomalies of up to 1.5°C are found off the west coast of northern Honshu (137°E, 40°N), where a significant decadal variability in the upper ocean heat content also has been observed [*Na et al.*, 2012]. The secondary maxima are found off the coast of the Korean Peninsula [*Yeh et al.*, 2010], as well as near the Tsugaru and Soya straits. The basin-averaged SST anomaly corresponding to ±1 standard deviation changes in the principal component (PC) time series is rather moderate, however, roughly ±0.3°C. The leading PC time series (red line in Figure 1d) shows a positive trend indicating a warming of the EJS in the last three decades [*Yeh et al.*, 2010]. It should be noted that the linear trend is not removed prior to the EOF calculation to be better compared with previous studies using longer data sets. The large-amplitude interannual variability is superposed onto the linear trend, resembling the interannual leading complex EOF mode of the upper ocean temperatures in *Minobe et al.* [2004]. The second mode, accounting for 18% of the variance, exhibits northeast to southwest tilted SST dipoles (Figure 1c), with the positive center off the east coast of Korea and the negative one west of Hokkaido. The area-averaged SST anomaly is close to 0°C. The second PC time series (blue line in Figure 1d) exhibits decadal variability with a positive peak in the mid-1990s preceded and followed by negative peaks in the late 1980s and early 2000s, mimicking the decadal leading complex EOF [*Minobe et al.*, 2004].

The EJS being a small marginal sea, these intrabasin structures of the SST anomaly are critical to the local air-sea interaction and the regional weather. An earlier study by *Chen et al.* [2001] compared the results from a weather forecast model forced with the Advanced Very High Resolution Radiometer (AVHRR) derived high-resolution SST with one forced with a smooth SST field from the National Centers for Environmental Prediction (NCEP)-National Center for Atmospheric Research (NCAR) Reanalysis [*Kalnay et al.*, 1996]. Monthly mean wind, turbulent heat flux, and precipitation were significantly influenced by the SST condition that resolves a sharp subpolar front. Similarly, using the data-assimilated SSTs, *Yamamoto and Hirose* [2008, 2009, 2010] demonstrated that mesoscale SST features improve the simulation of the regional winter atmospheric circulation associated with developing cyclones and cold air outbreaks.
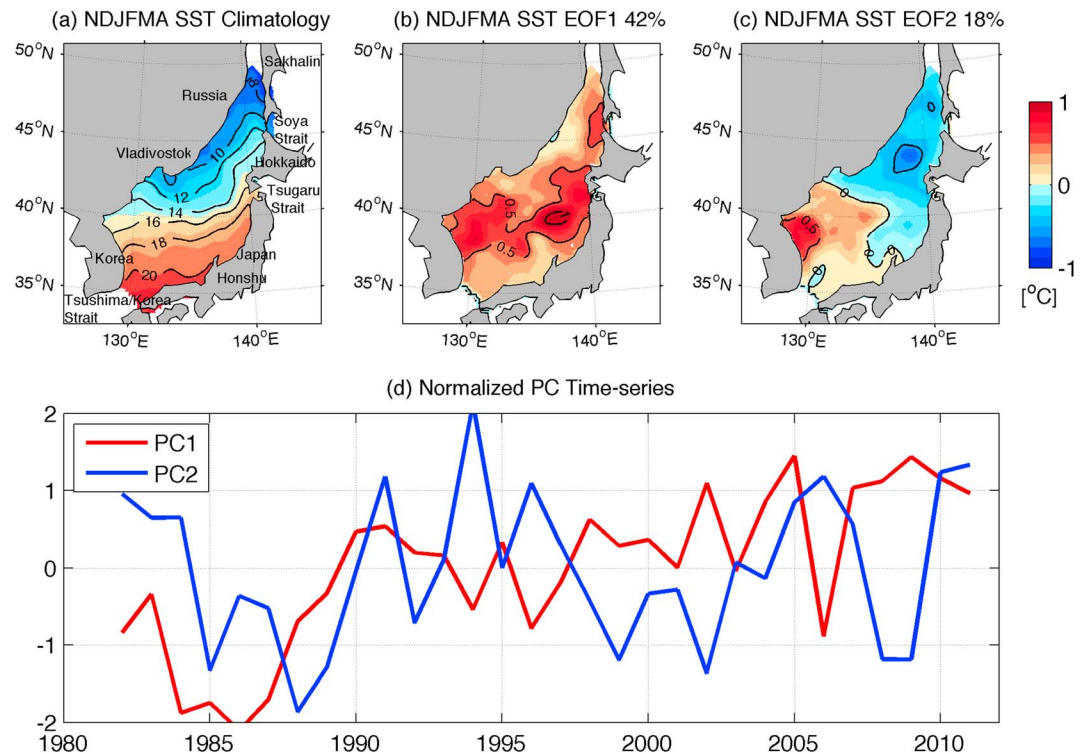
Figure 1. (a) Climatological (1982–2010) November–April (NDJFMA) mean EJS SST [°C, CI = 2°C]. (b–c) The first two modes of SST variability identified from the Empirical Orthogonal Function (EOF) analysis. The portion of the total variance explained by each mode is shown in the title. (d) The corresponding principal component (PC) time series. Amplitudes of the EOF patterns correspond to 1 standard deviation change in the respective PC time series.

In addition to the local impact, some aspects of large-scale atmospheric circulation appear to be sensitive to the EJS SST variability. *Yamamoto and Hirose* [2011] conducted twin experiments using a limited-domain atmospheric model forced with anomalously warm and cold EJS SSTs. They identified an amplified quasi-stationary trough over the Sea of Okhotsk as a result of increased baroclinicity and cyclogenesis when the EJS SST is anomalously low. This is, in part, consistent with the observational evidence put forward by *Hirose et al.* [2009] that the atmospheric circulation pattern that is coherent with the anomalous volume transport through the Tsushima/Korea Strait closely resembles the pattern associated with the Western Pacific (WP) teleconnections [*Wallace and Gutzler*, 1981]. Detailed dynamical mechanisms responsible for this correlation, however, remain unclear.

A more systematic modeling approach is needed to determine the dynamical process by which the EJS SSTs communicate with the local and large-scale atmospheric circulation. Given the significant degree of internal variability in the winter atmosphere and the moderate amplitude SST anomalies typical of the marginal seas, the longer integration and the larger ensembles are required in the atmospheric model simulation to assure robust signal detection. This study takes on the approach by the aforementioned classical AGCM studies on the effect of extratropical SST anomalies [e.g., *Kushnir et al.*, 2002], yet uses a multinesting regional atmospheric model to shed light on the scale interactions between a marginal sea and the basin-scale circulation. With a controlled set of experiments designed to address this problem, it is our interest to examine the extent to which the local and remote wintertime atmospheric circulation is sensitive to moderate amplitude SST anomalies in the EJS. In view of the fact that the EJS is much smaller than the midlatitude atmospheric Rossby deformation radius, we also aim to determine to what extent the intrabasin structure of the EJS SST anomalies is important for the large-scale atmospheric circulation. These questions will be addressed by comparing transient and equilibrium responses in local and remote circulation from the model simulations forced with various EJS SST anomaly patterns identified from the EOF analysis.

The paper is organized as follows. Section 2 describes the model and experimental setup. Section 3 compares the simulated climatology of the relevant fields to the observations. Section 4 examines the local response

adjacent to the forcing region. Section 5 discusses the nature of the remote response, followed by section 6, which identifies the dynamical process responsible for such a remote response. Section 7 is the summary and discussion.

2. Model Approach and Experimental Configuration

2.1. Modeling Approach

While the AGCMs have been frequently used in previous studies on the influence of extratropical SST anomalies (see the review by *Kushnir et al.* [2002]), their coarse horizontal resolution is particularly not well suited for the marginal sea study. The EJS has areal extent of roughly 10° by 10°, thus the typical resolution of the AGCMs of 1–2° or coarser would likely underestimate the small-scale SSTs and the narrow coastal orography that are important for wintertime precipitation [*Chen et al.*, 2001; *Yamamoto and Hirose*, 2009]. To better resolve these effects and their local and large-scale influences, the present study adopts a regional modeling approach based on the Weather Research and Forecast (WRF) [*Skamarock et al.*, 2008] including two-way dynamic downscaling and upscaling. WRF is configured for the Northern Hemisphere on a polar stereographic projection with multiple-nested domains covering different regions of interest. Information is interchanged across the lateral boundaries between the nested domains, whereby the solutions from the parent domain drive the process in the embedded domains via downscaling, while simultaneously the large-scale circulation is influenced by the process in the embedded domains via upscaling, the key process of our interest. The outmost domain (d01) at 180 km horizontal resolution covers the Northern Hemisphere (Figure 2a). The solutions from d01 successively interacts with the embedded domains at 60 km over the North Pacific Ocean (d02) and then with the innermost (d03) domain over the EJS at 12 km. This resolution in d03 is deemed adequate in resolving key features in the EJS [*Chen et al.*, 2001; *Yamamoto and Hirose*, 2009].

2.2. Experimental Configuration

Experiments described in this section represent idealized scenarios, in which the goal is to identify the dynamical process responsible for local and remote atmospheric response to the EJS SSTs in the absence of other atmospheric variability. The initial and lateral boundary conditions are obtained from a 6-hourly climatology (1970–2010) based on the NCEP-NCAR reanalysis. Climatology is chosen to facilitate straightforward comparisons among the SST perturbation runs described in the following section, independent of influence from the SST variability from the northwest Pacific [e.g., *Na et al.*, 2012] and from the tropics [e.g., *Horel and Wallace*, 1981; *Keshavamurty*, 1982; *Renwick and Wallace*, 1996; *Watson and Colucci*, 2002; *Wiedenmann et al.*, 2002; *Kwon et al.*, 2011]. Six-hourly climatology is prescribed at the lateral boundary of d01 only. The climatological condition for 1 November is used as the initial condition for the three domains.

Five sets of 40-member ensemble simulations are carried out, forced with five different types of SST. Each of the 40 ensemble members is initialized with the climatological initial condition on 1 November that is perturbed with a normally distributed random noise. Each run is then integrated for 6 months until 30 April. The control (CTL) simulation is the WRF model forced with the daily varying SST and sea ice extent climatology (1982–2010) from the NOAA OI ¼° SST (Figure 2a, green contours). A series of SST perturbation simulations is identical to CTL except that the SST boundary condition in d03 only includes time-invariant positive and negative anomaly patterns based on the first two EOF modes (Figures 1b and 1c) superposed onto the climatology (Figure 1a). Table 1 summarizes the details on the experimental setup. For example, EOF1P refers to the WRF forced with positive polarity of the first EOF pattern (Figure 2c) added to climatology (Figure 2b) in d03 only. Since the identical daily climatological sea ice extent and SST are prescribed outside the EJS domain in all cases, there is no boundary source of anomalous diabatic heating/cooling outside the EJS including the main storm track regions in the North Pacific.

2.3. Method of Analysis

Throughout the paper, the large-scale circulation response is examined in d01, which covers the entire Northern Hemisphere, whereas the local response is examined in d03 over the EJS. Unless mentioned otherwise, the response patterns are examined based on the ensemble mean (40 members) and time mean (NDJFMA) of differences between a perturbation run and the CTL (i.e., EOF1P-CTL). Ensemble difference is
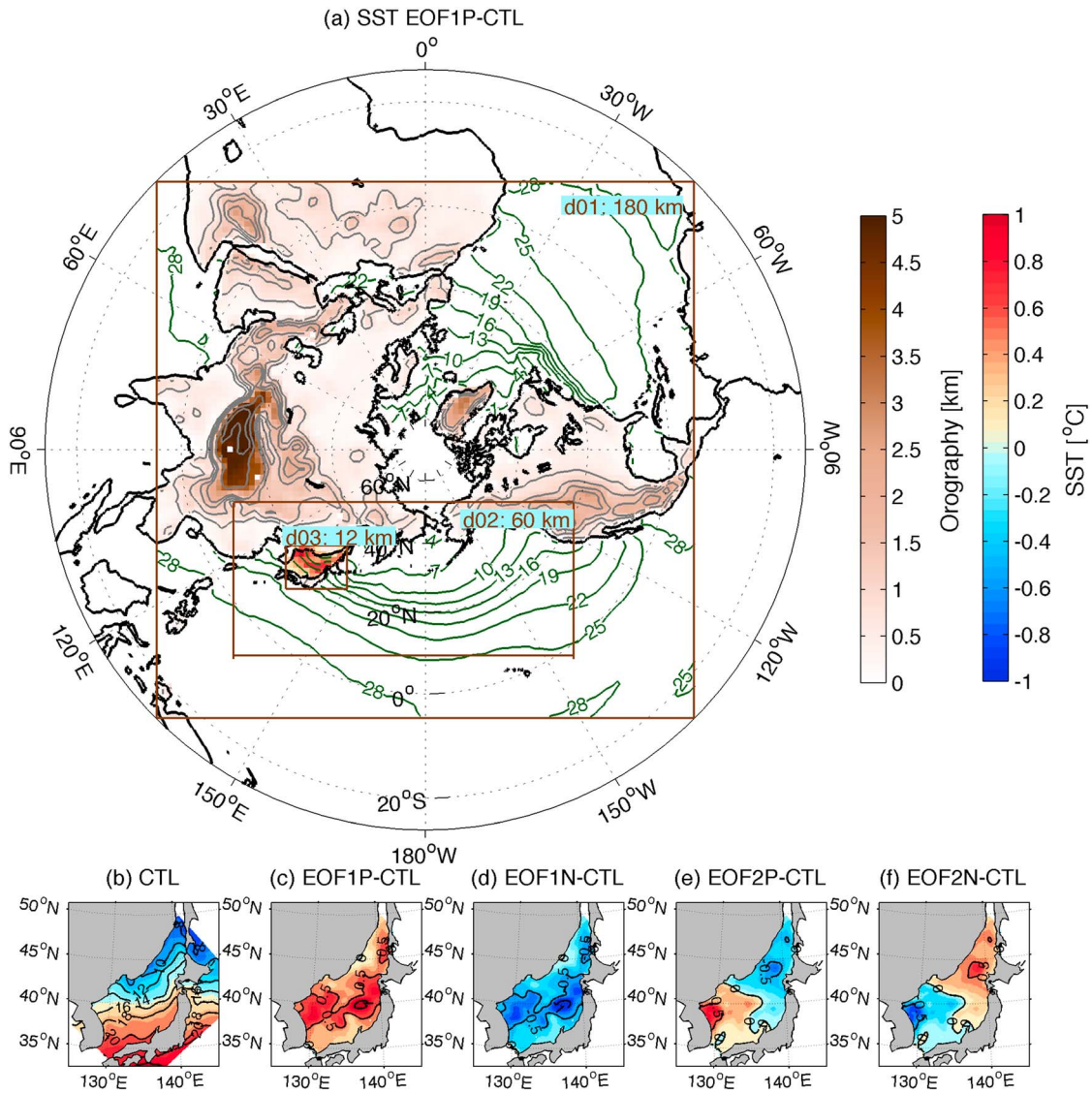
Figure 2. (a) Multinested WRF model domains (delineated by three brown boxes) covering the Northern Hemisphere on a polar stereographic projection. Green contours represent the climatological NDJFMA mean SST prescribed in the model domain. White-to-brown shadings and gray contours represent the orography ((km), CI = 0.5). The positive EOF 1 pattern of EJS SST is shown in the color shadings in domain 3 (d03). (b) The NDJFMA mean SST, which is used as the lower boundary condition for CTL simulation. SST anomalies added to the climatology in the subsequent SST perturbation simulations for (c) EOF1P, (d) EOF1N, (e) EOF2P, and (f) EOF2N.

calculated from the pair of runs sharing identical initial condition; therefore, there is no influence from the initial condition to the response. Statistical significance of the mean (variance) response is assessed by a two-sided Student's t test (F test). EOFs are computed from the area-weighted covariance matrix of the input time series, and are displayed as regressions on the corresponding normalized PC time series, so that the amplitude of the EOFs corresponds to one standard deviation change of the PC.

Table 1. The Names of the Experiments With the Types of SST Forcing

|	SST Forcing	Area-Averaged SST Anomaly
CTL	NDJFMA Climatology	N/A
EOF1P	NDJFMA Climatology + Positive first EOF pattern	+0.3°C
EOF1N	NDJFMA Climatology + Negative first EOF pattern	−0.3°C
EOF2P	NDJFMA Climatology + Positive second EOF pattern	0°C
EOF2N	NDJFMA Climatology + Negative second EOF pattern	0°C
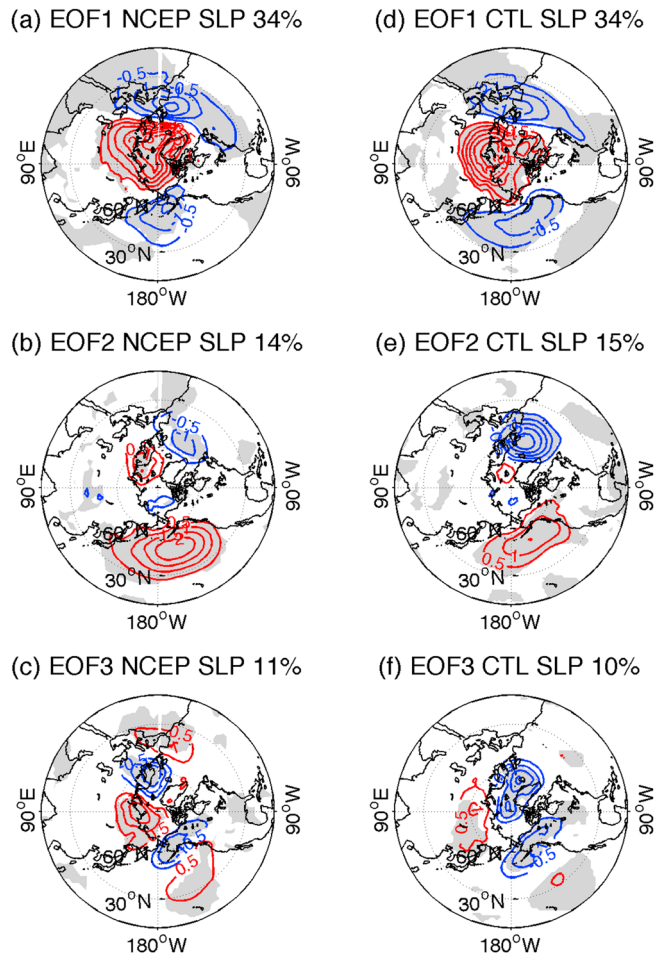
Figure 3. Leading EOF patterns of the NDJFMA-averaged SLP ([hPa], contours, positive red, negative blue) for (left) the 40 year NCEP-NCAR Reanalysis (NCEP hereafter) from 1970 through 2009 and (right) the 40-member ensemble CTL simulation. The influence of the tropical SST variability is removed in the NCEP SLP fields via regression prior to EOF analysis as explained in the text.

3. Model Validations

In order to examine the atmospheric response to extratropical SST anomalies, the model should reasonably well reproduce the dominant modes of large-scale circulation and the storm track climatology since the response is shaped by the interaction between the two. In this section, some relevant aspects of model simulation are compared to those derived from the NCEP-NCAR Reanalysis (hereafter NCEP).

Figure 3 compares the three leading EOF patterns of the NDJFMA mean sea level pressure (SLP) anomalies from NCEP with those from CTL. In NCEP, influence of the tropical SST variability is removed prior to the EOF analysis using a procedure similar to that by *Frankignoul et al.* [2011], as the model experiments are designed to exclude the tropical influence. Briefly, the component of SLP variability that covaries with the tropical SST variability is subtracted from the full SLP field by projecting SLP onto the first three PCs of the tropical Indo-Pacific (30°E–60°W 15°S–15°N) and then subsequently onto the tropical Atlantic (60°W–30°E, 15°S–15°N) SSTs. Considering the temporal lag between the tropical SSTs and extratropical SLP through the teleconnections, the tropical SST 1 month prior to our target period is used (October–March). This way, a more direct comparison of the dominant modes of NCEP SLP variability can be made with the model simulations with no tropical interannual variability [e.g., *Chu et al.*, 2013]. Note, however, that the model lacks the interannual variability of SST outside the EJS including those that may not be linearly correlated with the tropical SST variability, which may account for some discrepancy described here.
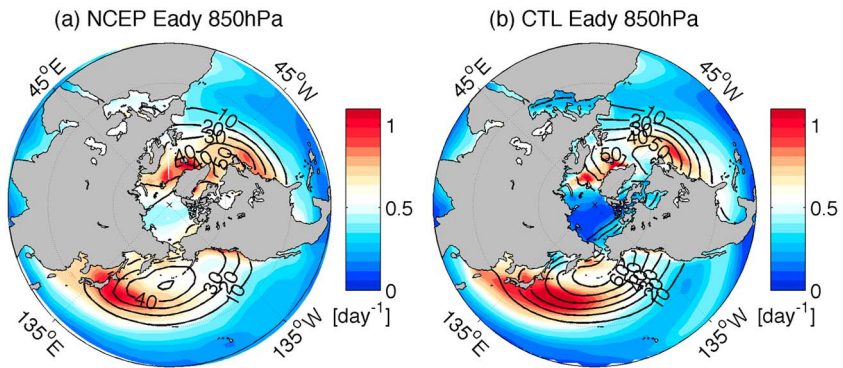
Figure 4. NDJFMA mean Eady growth rate at 850 hPa (shading, [day^{-1}]) from (a) the 40 year NCEP (1970–2009) and (b) the 40-member mean CTL simulation. The contours in each panel denote the NDJFMA mean variance of the 2–8 day band-pass filtered SLP [hPa^2], representing the climatological storm track.

The EOF patterns in CTL nonetheless agree surprisingly well with those in NCEP. The first modes in NCEP and CTL (Figures 3a and 3d) explain 34% of the total variances, resembling the Arctic Oscillation [*Thompson and Wallace*, 1998]. The second EOF modes, explaining 14–15% of the total variances, represent the variation of the intensity in the Aleutian Low (Figures 3b and 3e). The third EOF of CTL is also consistent with that of NCEP showing the wave train response linking the Gulf of Alaska and northern Siberia (Figures 3c and 3f).

CTL also reasonably represents the climatological low-level baroclinicity and intensity of the storm track. Figure 4 compares the Eady growth rate (σ, [day^{-1}]) estimated at 850 hPa level calculated by *Hoskins and Valdes* [1990] as

$$\sigma = 0.31 f \left| \frac{\partial \vec{v}}{\partial z} \right| \frac{1}{N},$$

where $N = \sqrt{\frac{g}{\theta} \frac{\partial \theta}{\partial z}}$ is the Brunt-Väisälä frequency, f the Coriolis parameter, θ the potential temperature, $\vec{v}$ the horizontal wind vectors, and g the gravitational acceleration. The climatological σ (shading) is overlaid in Figure 4 with the mean variance of the 2–8 day SLP (contours) representing the strength and path of the mean storm track. In NCEP, the areas of enhanced wintertime baroclinicity extend from the east coast of the Asian continent, passing over the East Asian marginal seas before attaining the maximum intensity in the northwest Pacific off Japan. The storm track extends from the region of the maximum σ off Japan toward the Bering Sea, where it reaches the maximum intensity of >50 hPa^2. The CTL simulation, while overestimating the strength of σ over the northwest Pacific Ocean, reproduces qualitatively similar climatology of low-level baroclinicity. The intensity of the storm track in CTL is also consistent with NCEP.

## 4. Local Near-Surface Atmospheric Responses

4.1. Climatology

The first step to identify the effect of anomalous diabatic heating or cooling would be to examine the atmospheric condition in the vicinity of the SST anomaly. Figure 5a shows the 10 m wind (W10, vectors) and the precipitation rate (shading) from CTL in November–January (NDJ), the period of maximum precipitation in this region. Strong northwesterly winds of continental origin (red vectors denoting wind speed >7 ms^{-1}), often associated with the wintertime cold air outbreaks, are impinged upon the mountainous Japanese coasts, generating large winter convective precipitation exceeding 15–20 mm day^{-1}. In much of the EJS basin, the mean northwesterly wind (vectors) tends to cross the isotherms of SST (black contours), facilitating a vigorous air mass modification process [*Manabe*, 1957]. The marine atmospheric boundary layer (MABL) is strongly coupled to SSTs [*Shimada and Kawamura*, 2006, 2008], resulting in the mean precipitation of 5–10 mm day^{-1} downstream of these features.

4.2. Response in the Near-Surface Wind to SST
4.2.1. Basin-Wide Modulation of Static Stability of the Atmospheric Boundary Layer

The local response in W10 is symmetric to the sign of SST anomalies. Figure 5b (Figure 5c) shows the accelerated (decelerated) northwesterly wind over warmer (colder) SST associated with EOF1P (EOF1N). The same
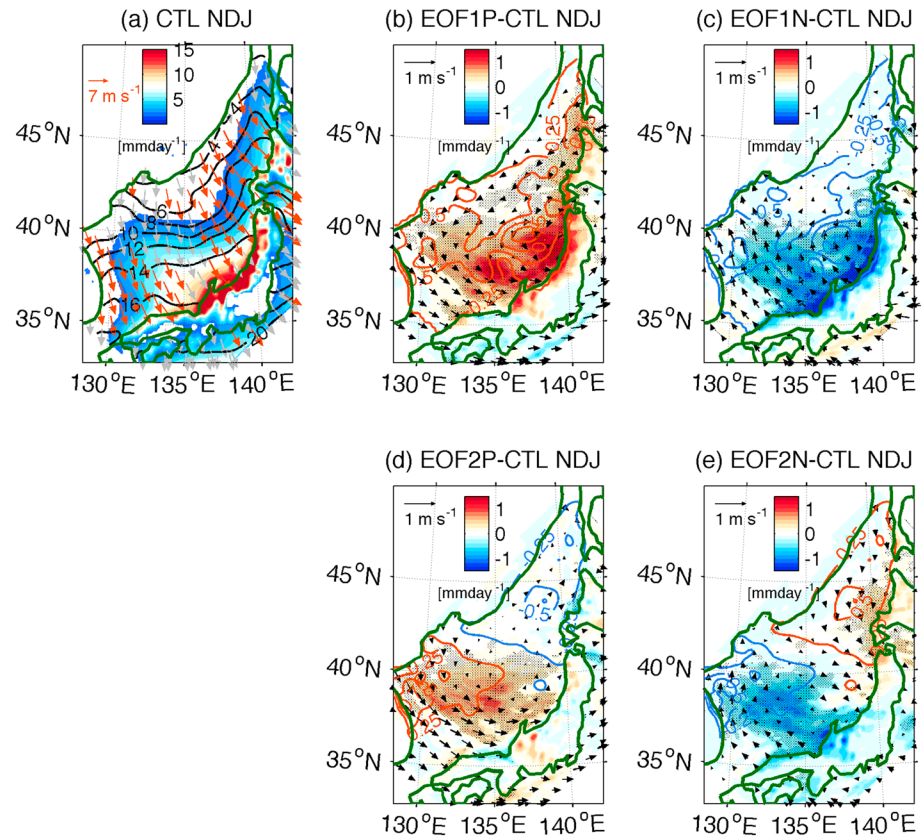
Figure 5. (a) November–January (NDJ)-averaged precipitation (shading, [mm day^{-1}]), 10 m wind vectors (W10, [m s^{-1}]) and SST (black contours, [°C]) from CTL. For clarity, precipitation less than 2 mm day^{-1} is not shown. Red (gray) vectors denote wind speed greater (less) than 7 m s^{-1}. Response in precipitation and wind to SST anomalies (red and blue contours) for (b) EOF1P-CTL, (c) EOF1N-CTL, (d) EOF2P-CTL, and (e) EOF2N-CTL. Dots represent the area of significant change in precipitation ($p = 0.05$). Vectors are plotted every nine grid points.

is true with the SST anomalies associated with EOF2P (EOF2N), showing anomalous northwesterlies (southeasterlies). A similar relationship between SST and the surface wind has been reported from the previous studies based on the in situ and satellite observations [*Shimada and Kawamura*, 2006, 2008] and the numerical models [*Chen et al.*, 2001; *Yamamoto and Hirose*, 2009; *Takahashi et al.*, 2013]. The apparent linearity in W10 response is further quantified in Figure 6 by the binned scatterplots of the SST anomalies and the W10 responses calculated over all the grid points in the EJS basin. In all four cases (Figures 6a and 6b), W10 exhibits statistically significant basin-wide linear response to the SST anomalies. The slope of the linear fit, also known as the coupling coefficient s, represents the effect of SST on the wind speed [e.g., *Chelton et al.*, 2004]. This coupling coefficient indicates that the basin-wide W10 response varies by +0.12 (+0.29) ms^{-1} due to +1°C variation SST anomalies associated with the EOF1P (EOF1N), and by +0.35 (+0.42) ms^{-1} for EOF2P (EOF2N).

The stronger overall W10 in the presence of warm (cold) SST anomalies in the EJS suggest that the EJS SST anomalies act to reinforce (suppress) the climatological northwesterly wind. This is in part due to the modulation of the statistic stability of MABL, which becomes more convectively unstable (stable) over anomalously warm (cold) SSTs. This stability modulation of the MABL can be demonstrated by comparing the basin-averaged vertical structure of the atmosphere. Figure 7a shows the vertical profiles of the potential temperature in EOF1P-CTL and EOF1N-CTL averaged over the EJS basin, superposed over the area-averaged height of the planetary boundary layer (PBLH, straight lines). Within the climatological PBL (black straight line), the potential temperature is higher (lower), with the maximum near the surface, in EOF1P (EOF1N) than that of CTL. Anomalously warmer near-surface temperatures would destabilize the MABL, leading to the higher PBL in EOF1P. The opposite is true with the colder SST. This stability adjustment within the MABL would in turn accelerate (decelerate) the surface winds [*Wallace et al.*, 1989; *Hayes et al.*, 1989; *Shimada and Kawamura*, 2006, 2008] via enhanced (reduced) downward turbulent transport of momentum to the surface
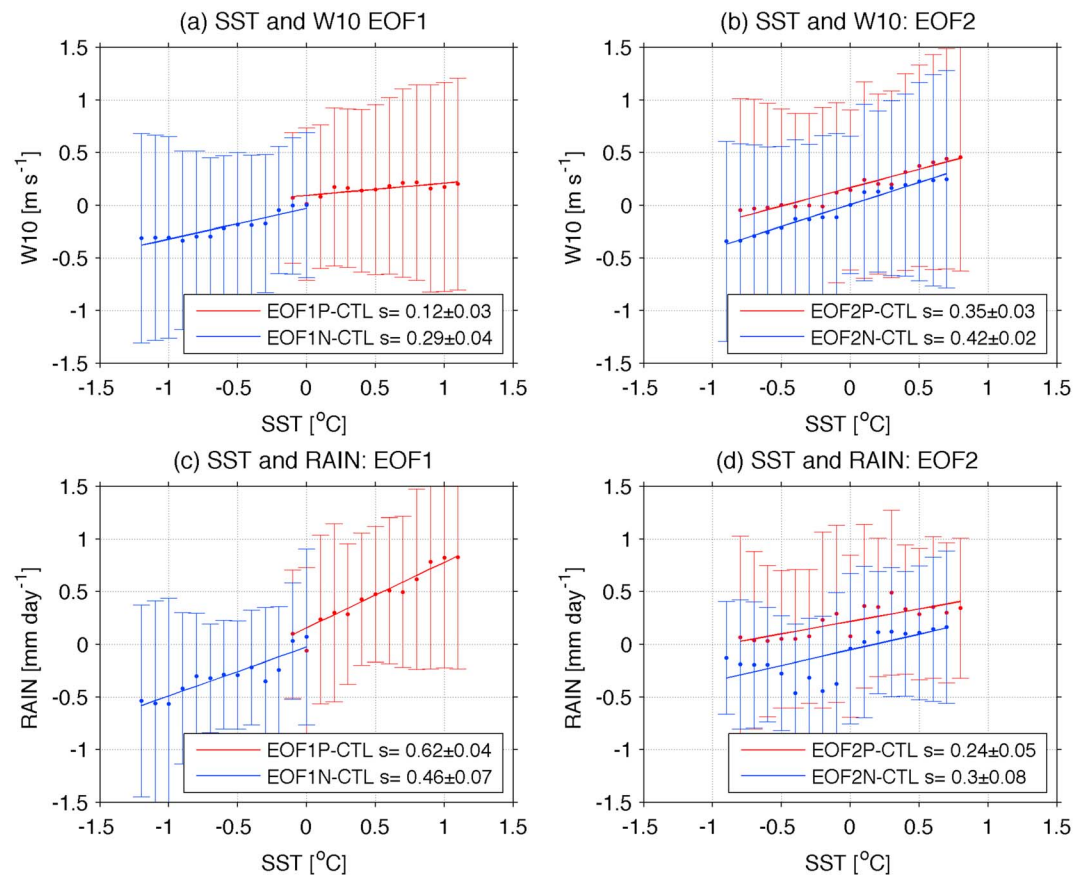
Figure 6. Binned scatter diagrams of the NDJ-averaged responses in (top) 10 m wind speed (W10, [m s^{-1}]) and (bottom) precipitation [mm day^{-1}] to SST anomalies [°C] in the EJS ocean grid point in d03 associated with (a) EOF1P-CTL, (b) EOF2P-CTL, (c) EOF1N-CTL, and (d) EOF2N-CTL. The dots represent the average in each bin, while the error bars represent corresponding ±1 standard deviation of the response. The straight lines denote the linear fit to the bin averages. The slope of linear fit (s) and the standard errors are shown in each panel. All slopes are statistically significant at $p = 0.05$.

over warm (cold) SSTs [e.g., *Chelton et al.*, 2001; *Nonaka and Xie*, 2003; *O'Neill et al.*, 2005; *Seo et al.*, 2007; *Small et al.*, 2008]. Figure 7b compares the corresponding profiles of the wind speed difference, showing the increase (decrease) in the low-level wind speed in EOF1P (EOF1N) within the PBL, consistent with the view that unstable lower atmosphere would enhance the near-surface wind. Stronger (weaker) northwesterly wind would in turn induce anomalously cold (warm) SST in the EJS, i.e., damping the SST anomalies, in nature and in coupled models. However, this damping effect is not accounted for in this study.

It should be noted from Figure 7 that the response in potential temperature and wind speed in the EJS domain is obviously a combination of linear response to the near-surface diabatic forcing and the nonlinear effect by the large-scale circulation change. The former is strongly manifested within the PBL closer to the surface forcing, while the latter is dominant in the upper level beyond the PBL, where the response is not symmetric. This is further discussed in section 5.

4.2.2. Adjustment of Sea Level Pressure on the Intrabasin SST Pattern

A closer examination of Figure 5 indicates the southward shift in the W10 response to the SST anomalies. This apparent quadrature relationship is better explained by the pressure adjustment mechanism [*Lindzen and Nigam* 1987], which suggests that the anomalous SSTs thermally induce a density (hence SLP) anomaly, leading to anomalous cross-frontal flows that diverge (converge) over the cold (warm) SST. To illustrate how well this mechanism explains the simulated phase relationship, the momentum budget analysis of vertically integrated linear MABL model by *Lindzen and Nigam* [1987] is carried out,
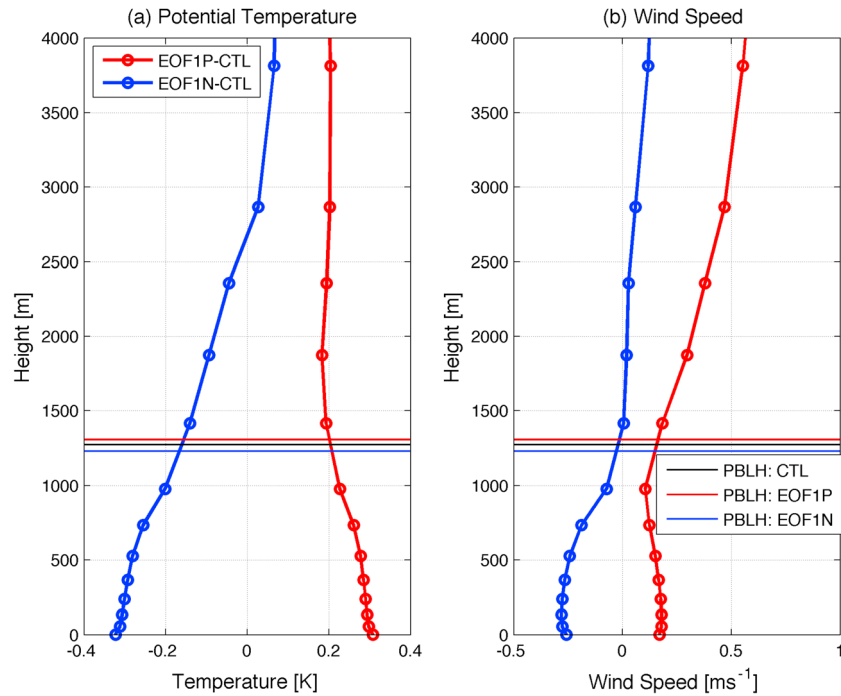
Figure 7. Difference in vertical profile in (a) potential temperatures [K] and (b) wind speed [ms^{-1}] averaged over the EJS domain (EJS water points only) from EOF1P-CTL (red) and EOF1N-CTL (blue). The thin red, black, and blue straight lines represent the area-averaged height of the planetary boundary layer in EOF1P (1.31 km), CTL (1.27 km), and EOF1N (1.23 km) in each case, respectively. The slope of linear fit (s) and the standard errors are shown in each panel. All slopes are statistically significant at $p = 0.05$.

which yields a linear relationship between the divergence (convergence) of W10 and the Laplacian of SLP, such that

$$\rho_o\left(\nabla \cdot \vec{u}\right) = -\left(\nabla^2 P\right)\frac{\varepsilon}{\varepsilon^2 + f^2},$$

where $\vec{u}$ denotes the horizontal 10 m wind vectors and ε the linear Newtonian damping coefficients [see also *Minobe et al.*, 2008; *Shimada and Minobe*, 2011; *Takatama et al.*, 2012]. The negative linear proportionality of $\nabla \cdot \vec{u}$ to $\nabla^2 P$ is suggested by this linear mixed layer model, which is clearly illustrated in Figures 8a and 8b by binned scatterplots, showing statistically significant negative linear relationships, in all cases, between $\nabla^2 P$ and $\nabla \cdot \vec{u}$. The spatial patterns of $\nabla^2 P$ and $\nabla \cdot \vec{u}$, visualized in Figures 8c and 8d for EOF1P-CTL case (other cases are similar, not shown), show the areas of negative (positive) $\nabla^2 P$ (Figure 8c) corresponding to the areas of divergence (convergence) of wind (Figure 8d). This response is linear such that the opposite response is obtained if the sign of SST anomaly is switched (not shown).

In summary, analysis of local wind response to the SST anomaly reveals two dynamically distinctive mechanisms for the SST-wind relationship that appear to be at work simultaneously, but on different spatial scales. In the basin-wide scale, SST anomalies modulate the MABL stability, giving rise to the in-phase and linear relationship between SST and W10. This is likely what would happen in the coarse-resolution AGCM models, which do not clearly resolve intrabasin SST structures. On this intrabasin scale, however, the apparent quadrature relationship between SST and W10 indicates the importance of the adjustment of SLP and the concomitant cross-frontal convergent and divergent flows associated with the SST anomalies [*Minobe et al.*, 2008; *Shimada and Minobe*, 2011]. More quantitative analysis is needed on the relative importance of two mechanisms (and the contribution from other processes, e.g., horizontal advection [*Small et al.*, 2003]) using a unified diagnosis approach to the MABL momentum budget [e.g., *Takatama et al.*, 2012].

4.3. Precipitation Response

The local response in precipitation also reflects the sign and pattern of the underlying SST anomalies, except that the precipitation response tends to be shifted downstream of the SST anomalies. Figure 5b shows the
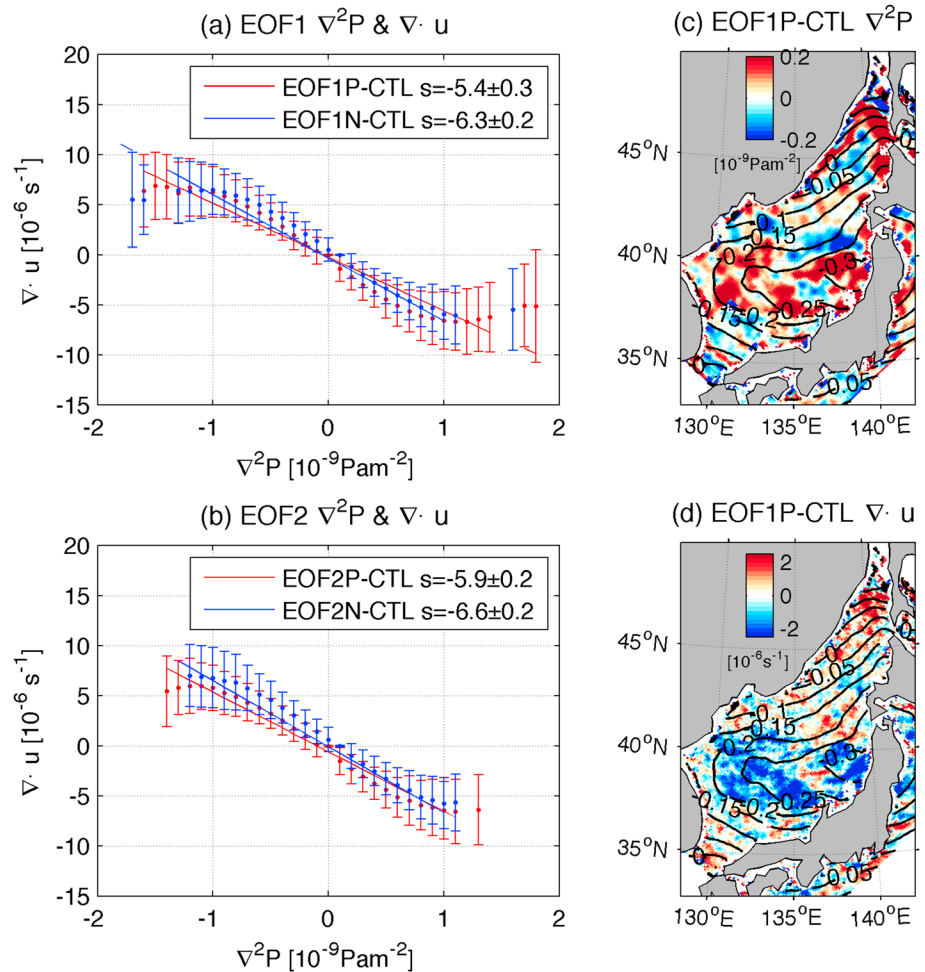
Figure 8. (a) Binned scatterplots of the NDJ-averaged Laplacian of SLP ($\nabla^2 P$, [10^{-9} Pa m^{-2}]) to the divergence of 10 m wind ($\nabla \cdot \vec{u}$, [10^{-6} s^{-1}]) from EOF1P-CTL (red) and EOF1N-CTL (blue). (b) As in Figure 8a except for EOF2P-CTL (red) and EOF2N-CTL (blue). All slopes are statistically significant at $p = 0.05$. (c) Spatial pattern in the NDJ-mean response in $\nabla^2 P$ in EOF1P-CTL overlaid with the response in SLP (black contours, [hPa], CI = 1 hPa). (d) As in Figure 8c except for $\nabla \cdot \vec{u}$ (positive denoting divergence).

response in precipitation (shading) from EOF1P-CTL reaching >2 mm day^{-1} over much of the basin, as well as in the stretch of the Japanese coast and downstream of the subpolar front. When the basin is filled with the EOF1N-type SST anomalies, the precipitation is reduced by about the same magnitude (Figure 5c). The same is true for the EOF2P and EOF2N, showing the shifted precipitation response downstream of the SST anomalies off the Korean coasts as well as the west coast of the Hokkaido and Sakhalin Islands. Despite the comparable amplitude and extent of the SST anomalies in the southern and northern portions of the basin (Figures 2e and 2f), the precipitation response is much stronger in the south. The greater precipitation response in the south might be due to the fact that the southern portion of the basin provides a greater fetch for the northwesterly wind, which would facilitate more enhanced response in precipitation via the air mass modification process. This greater fetch would also account for the stronger wind response in the southern limb of the SLP anomaly shown in Figure 5, suggesting that the SST anomalies in the southern portion of the basin might be particularly important for the local atmospheric response. The binned scatterplots for precipitation reveal somewhat less striking, yet still significant, linearity in the precipitation response (Figures 6c and 6d), indicating that other processes, including the advective process, can be important factors for determining the precipitation response pattern.

5. Large-Scale Atmospheric Response

The previous section identified the local response patterns providing dynamical explanations on the simulated local SST-wind-precipitation relationship. This section examines in detail the nature of the remote
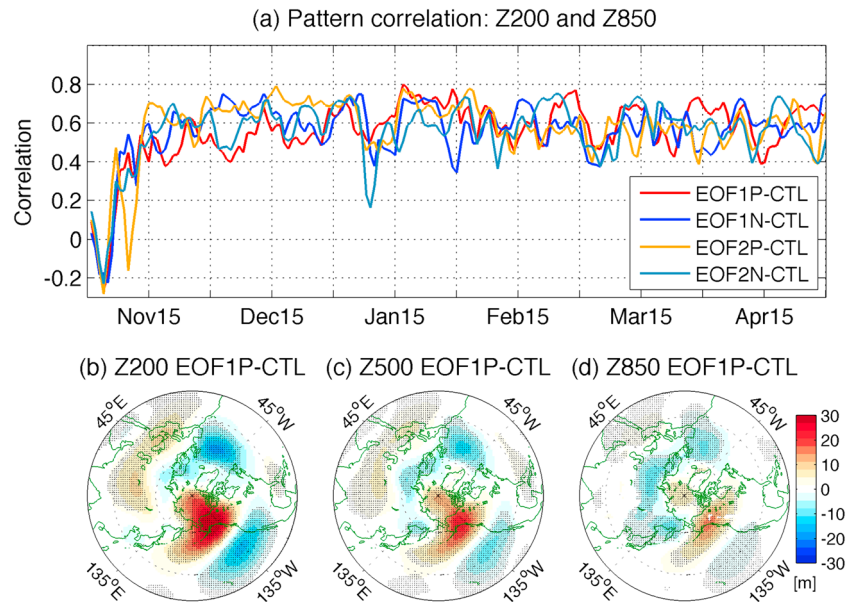
Figure 9. (a) Daily evolution of the pattern correlations between Z850 and Z200, color coded to represent the difference of the four perturbation runs from CTL. The equilibrium (NDJFMA mean excluding the first 15 days) response of EOF1P (i.e., EOF1P-CTL, [m]) in (b) Z200, (c) Z500, and (d) Z850. Dots denote the areas of significant ($p = 0.05$) change.

downstream response in the North Pacific and investigates key dynamical processes responsible for the remote response.

5.1. Temporal Evolution of Response

Figure 9a shows the daily time series of pattern correlation coefficients between the responses in geopotential height (Z) on 850 hPa and 200 hPa from d01, color coded to represent four perturbation cases. Denoted by a negative correlation between the lower and upper level height anomalies, the response pattern during the first 5 days (i.e., 1–5 November) is weakly baroclinic. This short-lived, initial baroclinic adjustment to the diabatic forcing is consistent with the linear response confined to the vicinity of the forcing [*Hoskins and Karoly*, 1981; *Li and Conil*, 2003; *Ferreira and Frankignoul*, 2005; *Deser et al.*, 2007; *Wang et al.*, 2012].

This initial adjustment period is followed by the rapid transition toward an equivalent barotropic structure denoted by the positive pattern correlations (~0.6–0.8) in all cases. Examination of the spatial response pattern in height fields at 200 hPa, 500 hPa, and 850 hPa for the EOF1P (Figures 9c–9d) further confirms the quasi-equilibrium equivalent barotropic structure with an anomalous ridge over Alaska and the anomalous trough in the northeastern Atlantic. The magnitude of height response is about 30 m, 20 m, and 10 m at the 200 hPa, 500 hPa, and 850 hPa level, respectively, which is within a comparable range of height response seen in the previous AGCM and coupled GCM studies [e.g., *Kushnir et al.*, 2002]. Note that the equivalent barotropic response is most pronounced in the Gulf of Alaska near the downstream of the Pacific storm track (Figure 4b), which appears as a common feature in all four cases but to a varying degree.

The transition from the initial response to the equilibrium is likely due to the transient synoptic eddies that feed on the low-level baroclinicity developed from the baroclinic response to diabatic heating anomalies [e.g., *Peng and Whitaker*, 1999]. Therefore, the transition timescale would depend on how factors such as the model's climatological storm track, the size/location of the SST forcing [*Hall et al.*, 2001], and the model's intrinsic variability [*Deser et al.*, 2007] are represented in the model. Previous studies based on different complexities and experimental models yield diverse estimates of the adjustment times, ranging from a very short initial response of 1–2 days as in *Li and Conil* [2003] to 2–3 weeks by *Deser et al.* [2007]. The particularly longer adjustment times in *Deser et al.* [2007] might be due to the low-resolution model (NCAR Community Climate Model version 3) used in their study (compared to that by *Li and Conil* [2003]), which may result in weaker transient eddy feedback. It may also be associated with the basin-scale and large-amplitude SST
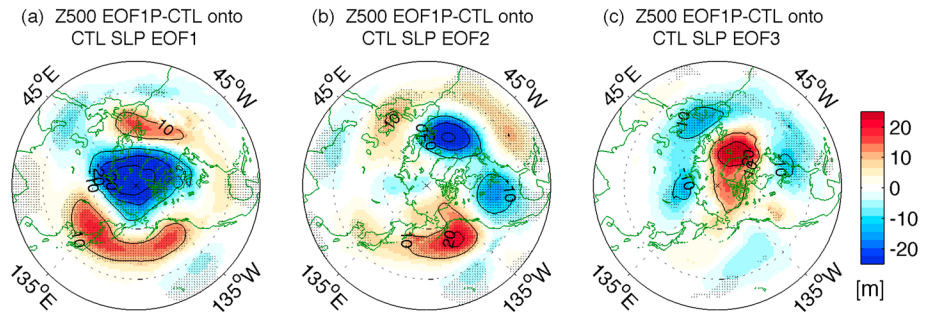
Figure 10. (a–c) The ensemble-averaged response in Z500 [m] from EOF1P-CTL projected onto the first 3 PCs of the SLP EOFs.

anomaly used in their experiments, which would amplify the initial baroclinic response to persist longer. Our experiments, in contrast, exhibit a much shorter adjustment period (1–5 days), which probably is related to the weak SST anomalies conducive to weak baroclinic response. This is, in fact, illustrated later in the paper (section 5.2, Figure 12) showing the extremely small response in the symmetric component of the Z500 response over the EJS. However, once a weak baroclinic response is generated, the storm track response rapidly and efficiently converts it into the equivalent barotropic ridge response. This rather efficient role by storm track in our study may be facilitated by the strong storm track variability featured in CTL (Figure 4b).

It is well known that the atmospheric response to the basin-scale extratropical SST anomalies projects onto the dominant modes of the atmospheric internal variability [e.g., *Peng and Robinson*, 2001; *Peng et al.*, 2003; *Magnusdottir et al.*, 2004; *Deser et al.*, 2007; *Cassou et al.*, 2007]. This is also the case with our EJS SST anomaly-forced experiments. In Figure 10, the mean Z500 response in EOF1P-CTL is regressed onto the first three PCs
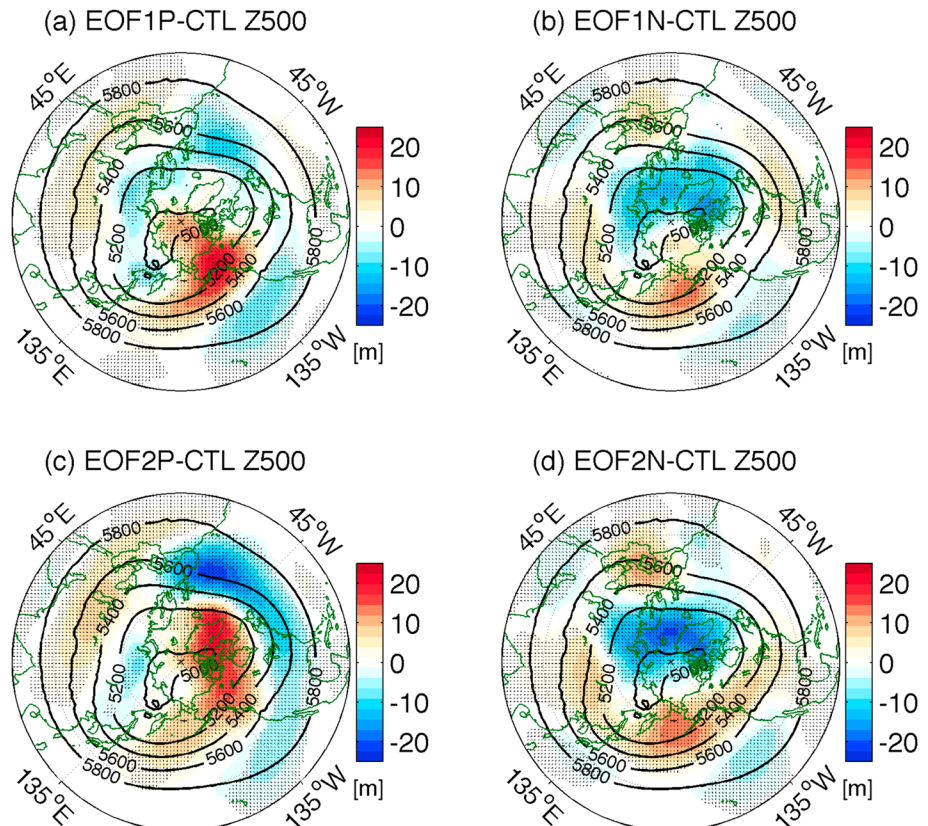
Figure 11. (a–d) Equilibrium response (NDJFMA averages) in 500 hPa geopotential height (Z500, [m], shading) overlaid with the NDJFMA mean CTL Z500 (black contours, CI = 200 m). Dots denote the areas of significant (*p* = 0.05) response in Z500.
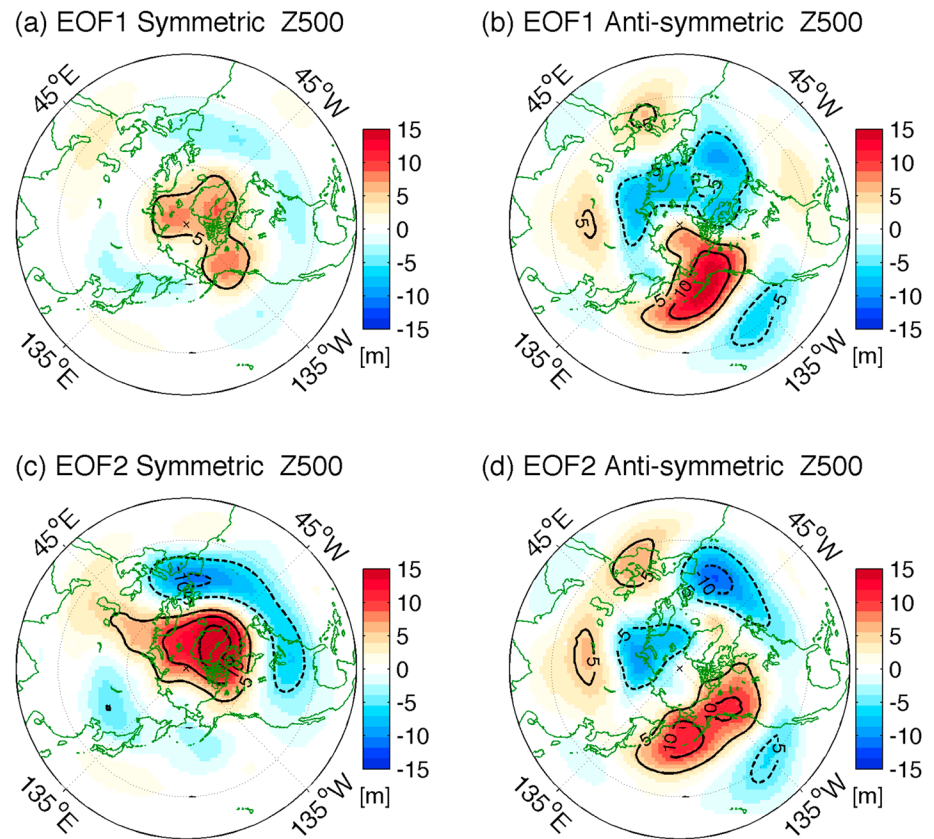
Figure 12. (a, c) Symmetric and (b, d) antisymmetric components of the NDJFMA mean response in Z500 ([m], CI = 5 m) with respect to the sign of EJS SST anomalies associated with (Figures 12a and 12b) EOF1 and (Figures 12c and 12d) EOF2.

obtained from the EOF analysis of CTL SLP (Figure 3). The equilibrium Z500 response (Figure 9c), having an anomalous ridge extending from the northwest Pacific toward the Gulf of Alaska and Chukchi/Beaufort Sea in the Arctic basin, bears a closer resemblance to the Z500 response projected onto the second PC than the first or third PCs. The pattern correlations between the mean Z500 response and the Z500 regressions are 0.07, 0.55, and −0.17 for PC1, PC2, and PC3, respectively. Therefore, in our study, the equilibrium response induced by the EJS SST anomalies is projected also onto the dominant modes of internal variability (the second mode in our case).

5.2. An Equilibrium Response

Figure 11 shows the map of ensemble mean response in Z500 averaged for the NDJFMA period (shading) in each of the four perturbation runs with respect to CTL, overlaid with the mean Z500 (contours) from CTL representing the climatological condition. Portions of the equilibrium response in the large-scale atmospheric circulation are, unlike the local response, apparently asymmetric with respect to polarity of SST forcing. In other words, independent of the sign and pattern of the specified SST anomaly, all four cases exhibit, to a varying degree, an anomalous ridge response near the Bering Strait and the Gulf of Alaska with amplitudes of up to 25 m. Another common ridge response is found in large areas across the Eurasian continent but with weaker amplitudes (<10 m). Anomalous trough response also emerges, again in all cases, in the subtropics of the eastern North Pacific.

The AGCM studies by *Pitcher et al.* [1988] and *Kushnir and Lau* [1992] discussed the nonlinear equilibrium response in height fields to SST anomalies of the opposite sign. The extent to which the equilibrium height response is linear or nonlinear can be assessed by decomposing the total height response to the component that is symmetric and antisymmetric [e.g., *Drévillon et al.*, 2003; *Li et al.*, 2007]. The symmetric response associated with EOF1-type SSTs can be approximated, for example, by ½ × (EOF1P − EOF1N), while the
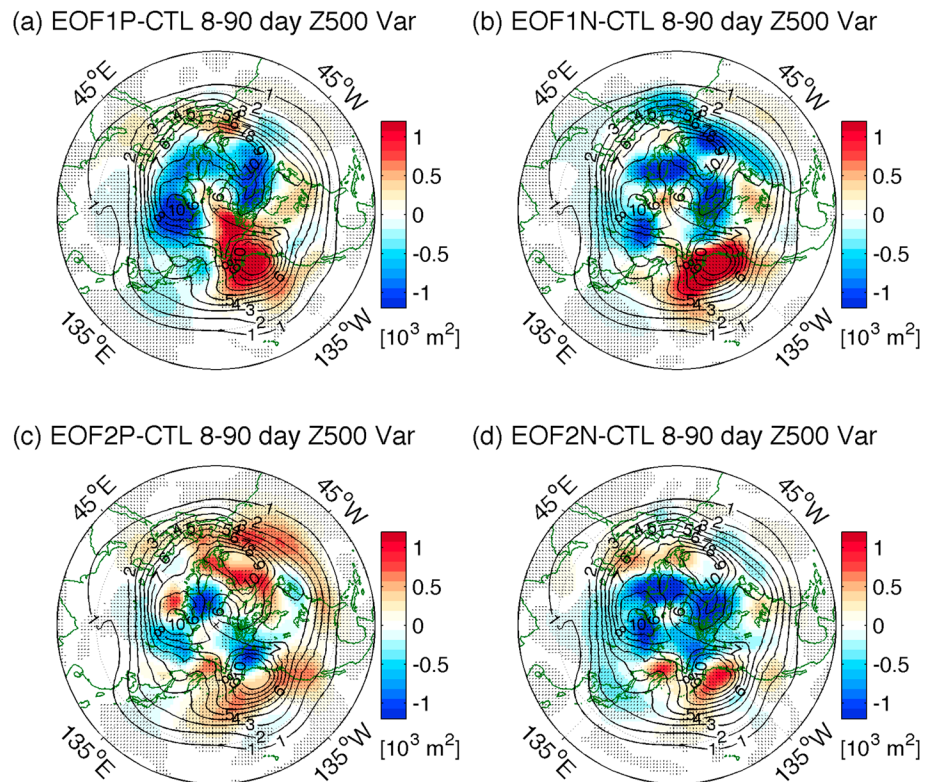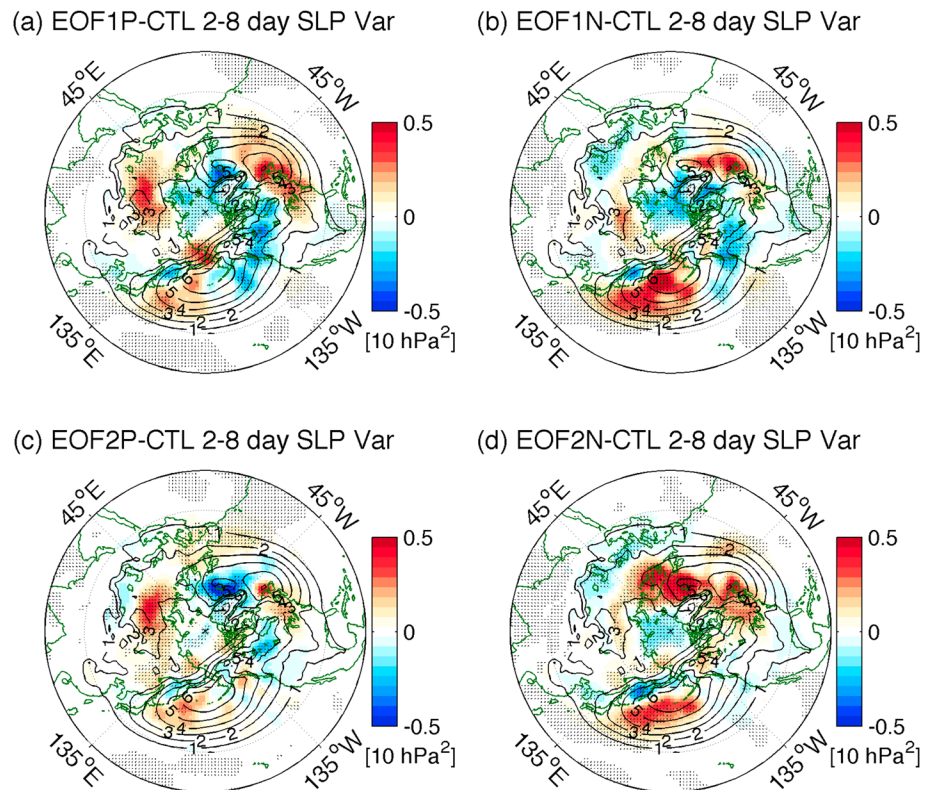
Figure 13. (a–d) Equilibrium NDJFMA response in the variance of 8–90 day filtered Z500 ([$10^3 m^2$], shading) overlaid with the variance of 8–90 day filtered Z500 in CTL (black contours, CI = $10^3 m^2$). Dots denote the areas of significant ($p = 0.05$) response in the 8–90 day Z500 variance.

antisymmetric component is derived by ½ × (EOF1P − CTL + EOF1N − CTL). The same procedure is applied to EOF2 SSTs. Figure 12 compares the symmetric and antisymmetric components of the Z500 response for the EOF1 and EOF2 SST experiments. Evidently, the equilibrium Z500 response to the positive and negative EOF1 SSTs (Figures 11a and 11b) bears a strong resemblance to the antisymmetric component of the total response (Figure 12b) with an anomalous ridge >15 m in the Gulf of Alaska extending from the northwest Pacific, rather than the symmetric response with a weak ridge response of 5–10 m over the Arctic basin. A weak ridge response across the Eurasian continent and the trough in the subtropical eastern North Pacific are also identified as the nonlinear response. The anomalous ridge response in the North Pacific to positive and negative EOF2 SSTs (Figures 11c and 11d) is also dominated by the antisymmetric response there (Figure 12d), although in this case, the symmetric response remains large (>15 m) over Greenland. This comparison indicates that the total equilibrium equivalent barotropic high response in the Gulf of Alaska is dominantly nonlinear. The remainder of this study will discuss the mechanism for the dominant nonlinear equilibrium response in the Gulf of Alaska.

5.3. Synoptic and Intraseasonal Transient Eddy Variability

The anomalous ridge response fluctuates primarily on the intraseasonal (8–90 day) timescale as revealed by spectral analysis of daily Z500 (not shown). Figure 13 shows the map of the response in variance of the 8–90 day filtered Z500 (shading) overlaid with the variance of the climatological 8–90 day Z500 from CTL (contours). The CTL climatology reveals the anticyclonic ridge in the Gulf of Alaska as the most prominent center of the climatological blocking in the North Pacific. The response in the intraseasonal height anomaly indicates the increased intensity of the climatological blocking there, which is more pronounced with EOF1P and EOF1N, and to a lesser degree with EOF2P and EOF2N. Changes in blocking intensity in the eastern North Atlantic and Siberia are not consistent across the model runs, and hence not discussed. The response in blocking anticyclones persists long enough to influence the ensemble mean and time-mean response in the winter atmospheric circulation (Figure 11), which also can be seen in the leading EOFs of SLP (Figure 3).
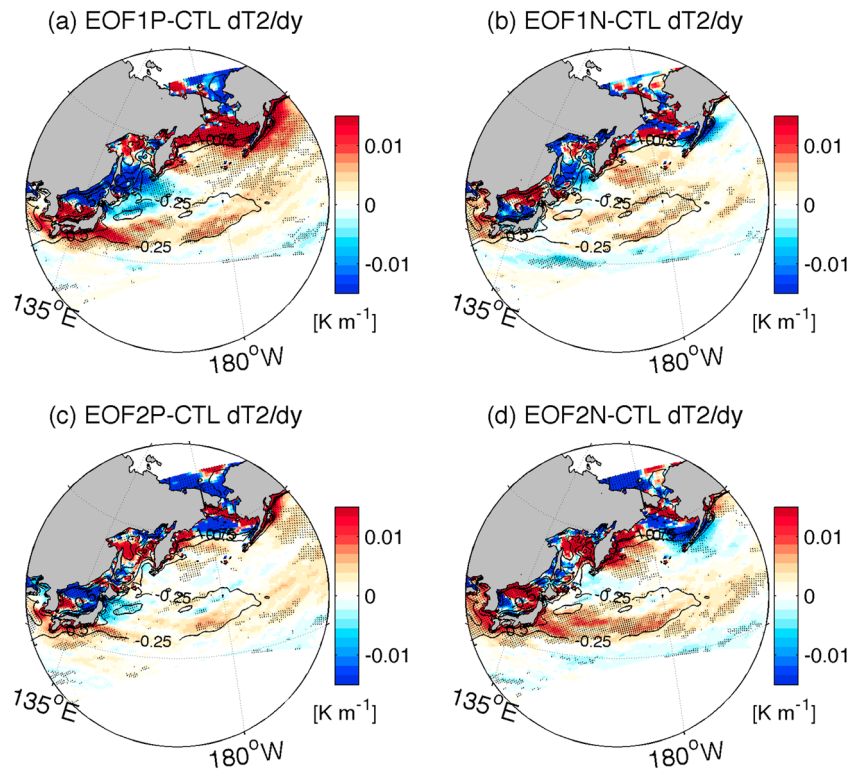
Figure 14. (a–d) Equilibrium NDJFMA response in the variance of 2–8 day filtered SLP ([hPa^2], shading) overlaid with the variance of 2–8 day filtered SLP in CTL (black contours, CI = 10 hPa^2). Dots denote the areas of significant ($p = 0.05$) response in the 2–8 day SLP variance.

This enhanced blocking response in the downstream is accompanied by the enhanced synoptic-scale variability in the northwest Pacific. Figure 14 shows the response in variance of the 2–8 day filtered SLP (shading) superposed with that in CTL (black contours). Synoptic transient eddy activity in the upstream of the climatological storm track in the northwest Pacific is enhanced significantly, independent of the sign and amplitude of SST anomalies. It appears that the colder SSTs in the southern portion of EJS (EOF1N and EOF2N) lead to a stronger enhancement of synoptic eddy activity and a southward shift in the storm track. This appears to be due to the enhanced near-surface baroclinicity in the southern EJS basin. Figure 15 shows the NDJFMA mean difference in a meridional gradient of air temperature (d$T2$/dy, negative denoting increased near-surface baroclinicity) overlaid with its climatology from CTL. Note that Figures 15–17 show the results from d02 to better visualize the response in the EJS and the western North Pacific. In the EJS, the change in d$T2$/dy (shading) closely reflects the meridional gradient of the prescribed SST anomaly pattern (Figures 2c–2f). The colder SSTs in the southern basin associated with the EOF1N and EOF2N reduce the d$T2$/dy there (i.e., increase in near-surface baroclinicity), accounting for the apparent southward shift in the storm track in EOF1N and EOF2N (Figures 14b and 14d). When the EOF1P and EOF2P-type SST anomalies are prescribed, the southern (northern) basin exhibits a decreased (increased) near-surface baroclinicity (Figures 15a and 15c), leading to not as significant southward intensification of the storm track as seen in Figures 14a and 14c.

Figure 16 shows the changes in Eady growth rate (σ) at 850 hPa. In the EJS, EOF1P, and EOF2P SSTs, increase σ in the northern basin (Figures 16a and 16c), where the near-surface baroclinicity is also increased (Figures 15a and 15c). Note that baroclinicity at 850 hPa level (d$T850$/dy) shows the similar pattern and sign changes to d$T2$/dy (not shown). Hence, the increased near-surface baroclinicity associated with the EOF1P and EOF2P-type SST anomalies leads to the locally increased Eady growth rate in the lower troposphere. EOF1N and EOF2N SSTs, in contrast, yield a basin-wide uniform reduction in σ (Figures 16b and 16d) despite the dipolar pattern in near-surface baroclinicity (Figures 15b and 15d). In this case, d$T850$/dy is also increased uniformly in the EJS (not shown). This indicates that the direct linear response to the EOF1N and EOF2N-type SST anomalies is shallower, mainly limited within the PBL, because of the dominant effect by the nonlinear

Figure 15. (a–d) Equilibrium NDJFMA response in the meridional gradient of 2 m air temperature (d$T$2/dy, [°C 10^{-5} m^{-1}], shading) overlaid with the climatological mean d$T$2/dy (black contours, CI = 0.25°C 10^{-5} m^{-1}). Dots denote the areas of significant ($p = 0.05$) change. Note that the positive (negative) change in d$T$2/dy indicates the decrease (increase) in near-surface baroclinicity.
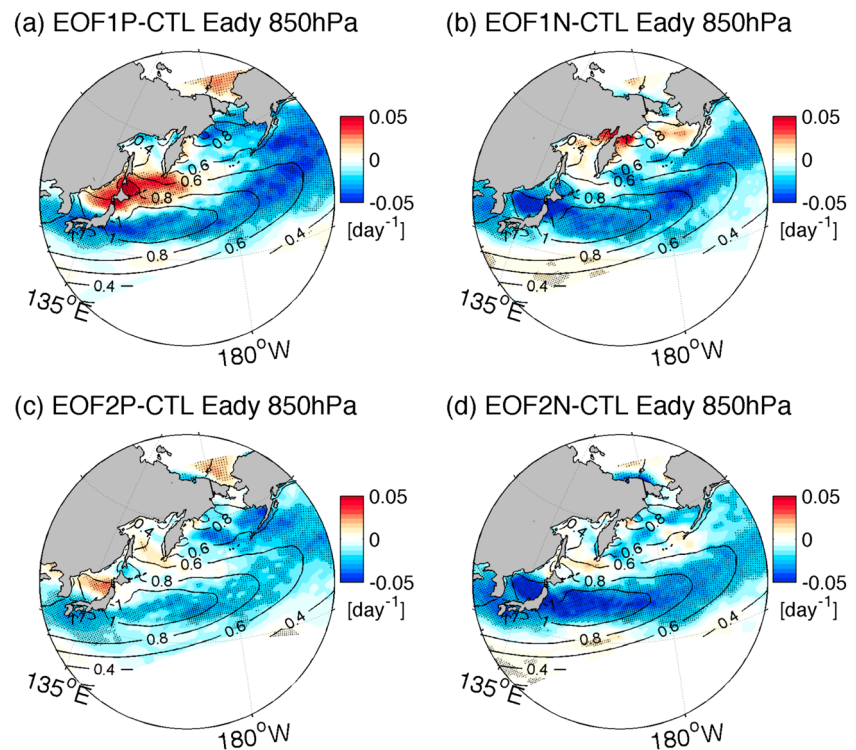
Figure 16. (a–d) Equilibrium NDJFMA response in the Eady growth rate (σ, [day^{-1}], shading) at 850 hPa overlaid with the climatological mean 850 hPa σ (black contours, CI = 0.2 day^{-1}). Dots denote the areas of significant ($p = 0.05$) change.
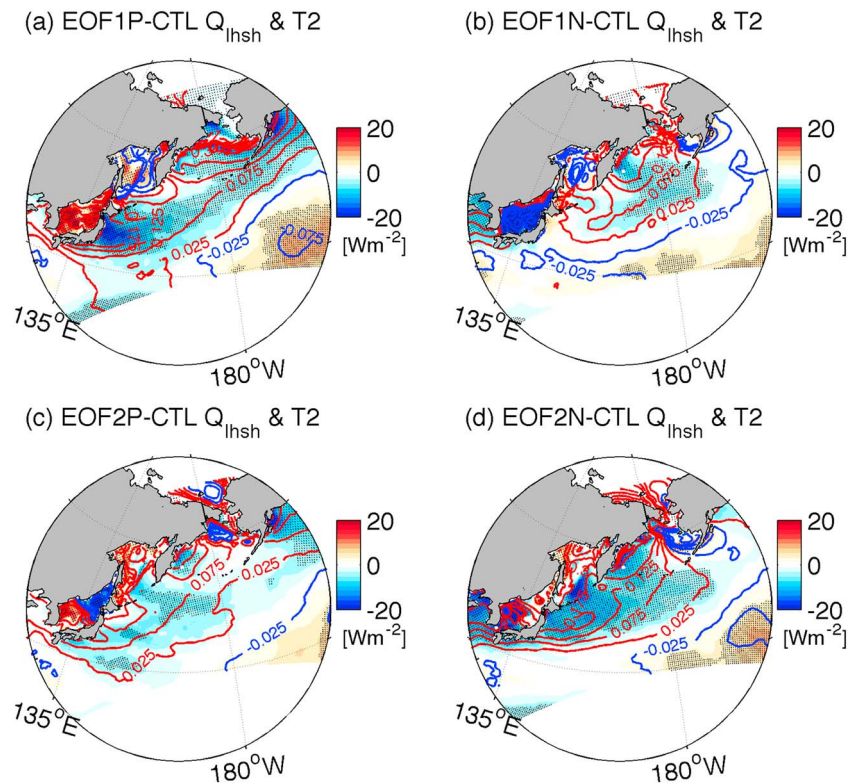
Figure 17. (a–d) Equilibrium NDJFMA response in net turbulent heat flux (Q_{lhsh}, [W m^{-2}, negative cooling the atmosphere]) overlaid with the NDJFMA response in T2 (contours, [°C]). Red (blue) contours denote the increase (decrease) in $T2$ (with CI = 0.05 °C). Dots denote the areas of significant ($p = 0.05$) change in Q_{lhsh}.

circulation changes prevailing in the upper level (e.g., Figure 7), producing increased storm track response (Figures 14b and 14d).

Farther in the downstream of the EJS over the main storm track region, where the storm track intensities were generally increased (Figure 14), the near-surface baroclinicity and the Eady growth rates are reduced in all four cases (Figures 15, 16). Considering that there is no local diabatic forcing in the Kuroshio-Oyashio Extension (KOE) region in our model, this decrease in near-surface baroclinicity with the increased storm track variability should be viewed as the latter causing the former via meridional heat transport by storms. This is in line with the anomalously increased $T2$ in the KOE region in all four cases (Figure 17, contours). The increased surface turbulent heat flux anomalies (Figure 17, blue shading denoting cooling the atmosphere) act to reduce (instead of drive) the increased $T2$ anomalies over the subpolar side of the KOE fronts. This corroborates the idea that the decreased baroclinicity and the increased $T2$ in the main storm track region is a dynamical consequence of the increased storm track variability arising from the EJS SST anomalies.

6. Transient Eddy Flux Forcing and Time-Mean Circulation Response

6.1. Evolution of Anomalous Synoptic and Intraseasonal Eddies

It has been suggested that the enhanced low-frequency blocking anticyclones in the downstream of the climatological storm track are accompanied by the increased synoptic transient eddy activity in the upstream, via synergistic eddy-mean flow interactions [e.g., *Shutts*, 1983; *Dole*, 1986; *Blackmon et al.*, 1986; *Haines and Marshall*, 1987; *Nakamura and Wallace*, 1990, hereafter NW90]. NW90, in particular, demonstrated that this enhanced baroclinic wave activity in the upstream is primarily a manifestation of deeper cyclones at the surface. Following the anomaly composite method by NW90, the envelope function of synoptic transient eddy activity based on SLP is constructed, which essentially represents the variance anomaly time series associated with the transient baroclinic waves. A detailed procedure is outlined in NW90.
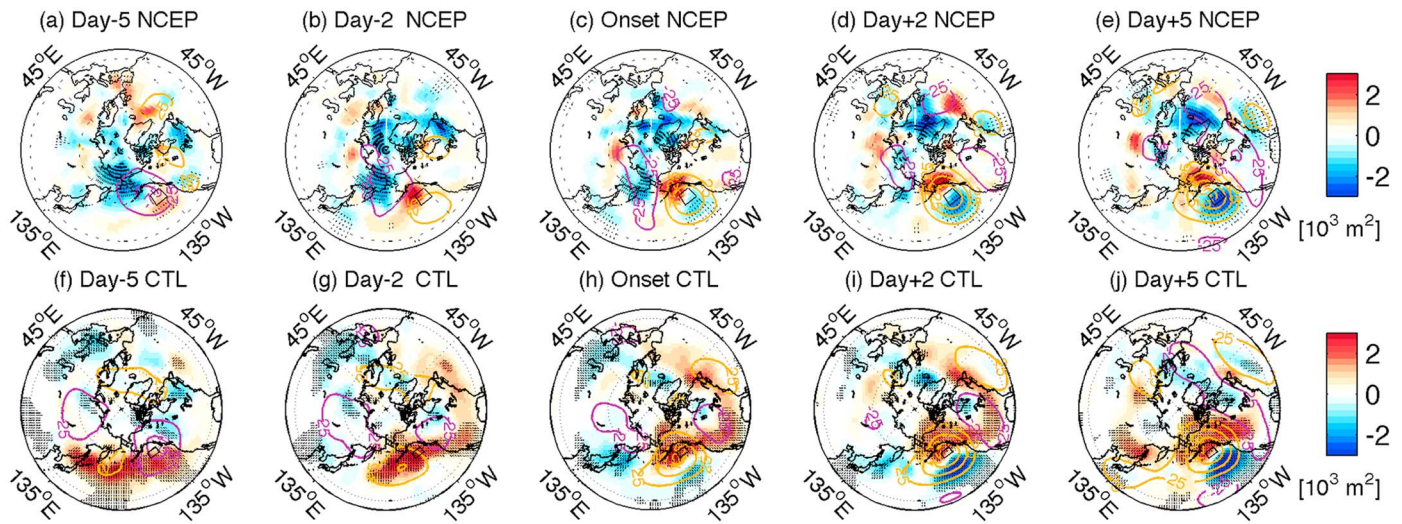
Figure 18. (a–e) Lead/lag composite evolution of the 2–8 day variance anomalies of the NCEP Z500 (shading, [m^2]), i.e., the envelope function representing the intensity of synoptic baroclinic wave activity, overlaid with the low-frequency (8–90 day) Z500 (contours, orange for positive, purple for negative, [m], CI = 50 m). Forty year (1970–2009) NDJFMA daily Z500 fields are used for the composite analysis. A total of 59 cases were classified as the blocking episodes at 50°N, 140°W (black box). The composites are relative to the onset of the positive blocking episode. Negative (positive) days correspond to prior (after) the onset of blocking. Dots denote the areas of significant composite anomalies ($p = 0.05$) of the envelope function. (f–j) As in Figures 18a–18e but for CTL based on 40 members. A total of 65 cases were identified as blocking episodes.

This synoptic envelope function, together with the 8–90 day filtered Z500 representing intraseasonal transient eddies, is composited in time with respect to the Gulf of Alaska blocking index, which is defined simply as the time series of 8–90 day filtered Z500 at 50°N, 140°W (black boxes in Figures 18–20). As in NW90, the onset of a block (Day 0) is defined as the first day of the Alaskan blocking time series that continuously exceeds the prescribed threshold value (half the standard deviation) and lasts at least 10 days. Day 0 represents the most rapid evolution of intraseasonal circulation, and the leads (lags) denote the circulation anomalies associated with synoptic and intraseasonal transient eddies prior to (after) the onset of a block. The methodology allows for a concurrent view of the relationship between synoptic baroclinic eddies and intraseasonal blocking anticyclones by capturing relatively rapid evolution of the onset and decay of a block [*Dole*, 1989]. This anomaly composite method is applied first to the 40 year NCEP reanalysis and the 40-member CTL simulation. Figure 18 shows that, both in NCEP (top) and CTL (bottom), above-normal synoptic transient eddy activity (reddish shading) appears in the central North Pacific in Day -5. In Day -2, as
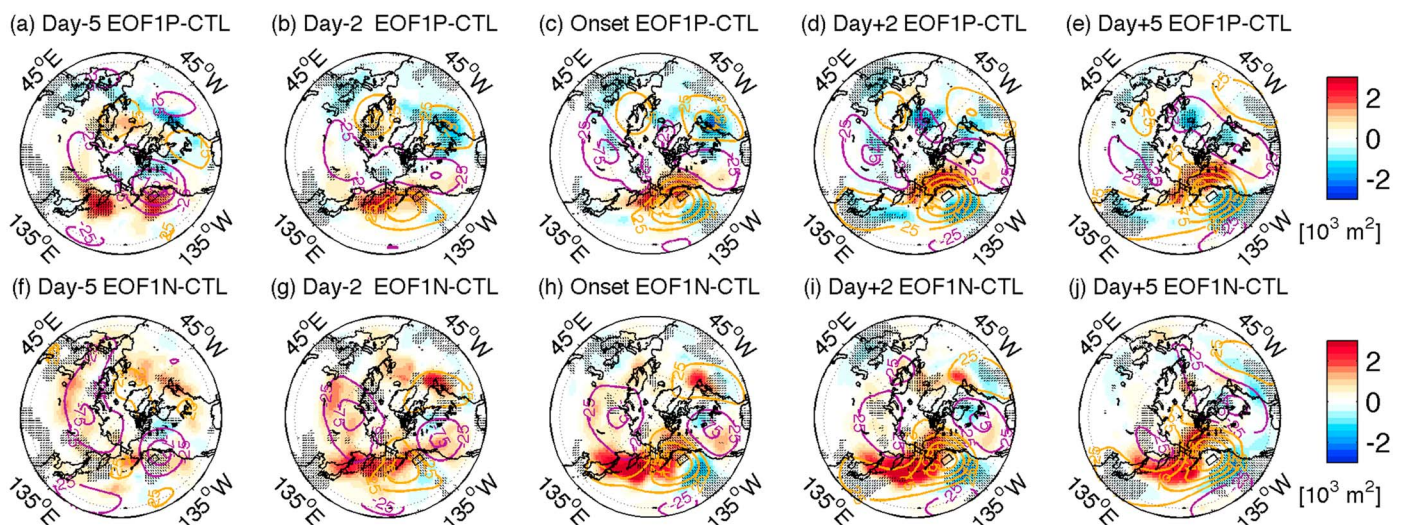
Figure 19. Same as in Figure 18 but for (a–e) EOF1P-CTL and (f–j) EOF1N-CTL. The total numbers of cases classified as blocking episodes are 62 and 60 for EOF1P-CTL, and EOF1N-CTL, respectively.
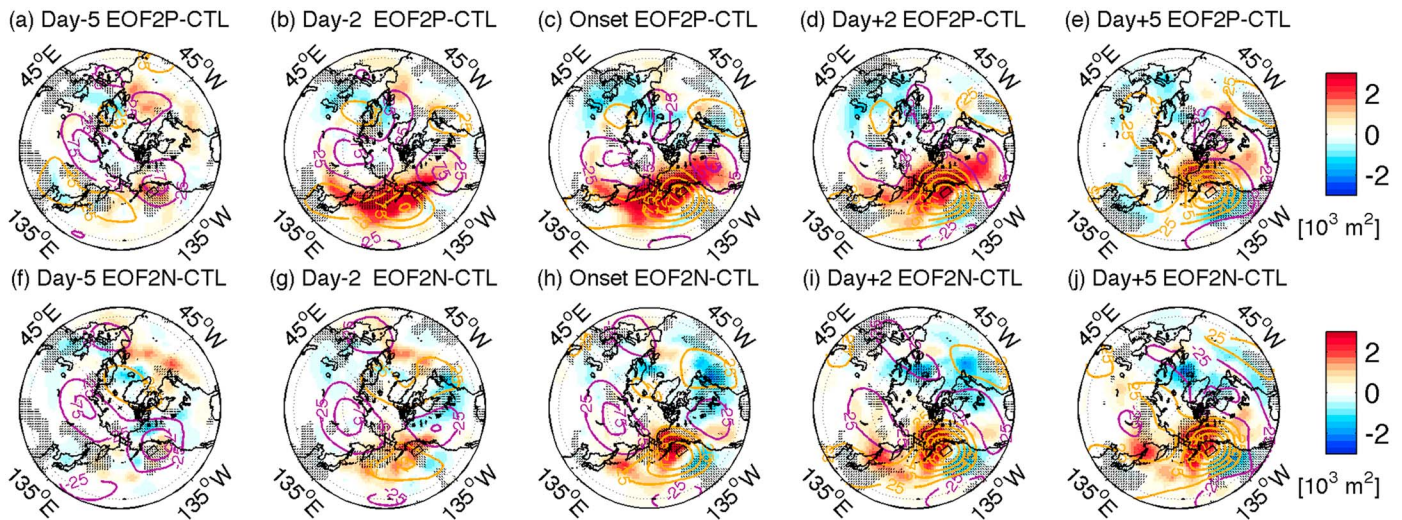
Figure 20. Same as in Figure 18 but for (a–e) EOF2P-CTL and (f–j) EOF2N-CTL. The total numbers of cases classified as blocking episodes are 53 and 54 for EOF2P-CTL and EOF2N-CTL, respectively.

the block is being formed (orange contours) in the Gulf of Alaska, this enhanced synoptic eddy activity is steered to the north of the developing blocking center, while anomalously reduced (bluish shading) to the south. The onset of a block (Day 0) is associated with this baroclinic wave activity attaining large positive amplitude north of the anticyclone ridge, while the suppressed one in the vicinity and to the south of the center. This is consistent with a picture of the split westerlies due to the amplification of the blocking [*Nakamura et al.*, 1997]. In Day +2 and Day +5, the positive and negative anomalous synoptic variability attains the maximum intensity. The amplitude of the envelope function in NCEP is smaller than that of CTL, yet the temporal covariation between the envelope function and the low-frequency circulation is qualitatively consistent.

In Figures 19 and 20, the same procedure is applied to the response fields. In EOF1P-CTL (Figure 19, top), the baroclinic wave activity is particularly pronounced over the Sea of Okhotsk and the Bering Strait in Day -5 and Day -2. Once the block is formed in Day 0, the blocking anticyclone response co-occurs with the amplified baroclinic wave activity in northern Alaska and the suppressed one in the south, consistent with the composite evolutions of the full field in NCEP and CTL. This relationship is rather well reproduced in all other cases, suggesting that if SST anomalies of any sign and pattern exist in the EJS, the downstream transient eddy activity is enhanced over the northwest Pacific. The connection between local SST and transient eddy activity is likely through the baroclinic response induced by the diabatic forcing and the resultant increase in near-surface baroclinicity (Figure 15) in the EJS. This would lead to the increased synoptic baroclinic wave activity (Figure 14) in the northwest Pacific. This composite analysis also suggests the association of the increased baroclinic wave activity to the amplification of the blocking ridge in the Gulf of Alaska with a few days lag. However, this composite analysis does not allow determining, conclusively, the causal relationship between the two. In the following section, further evidence is provided to show that the common anomalous ridge response in Figure 11 owes much of its existence to changes in upstream transient synoptic eddy variability via the storm track shift.

6.2. Vorticity Flux Convergence by Synoptic Eddies

The nonlinear equilibrium response, according to the previous studies, is likely associated with eddy vorticity flux turning the direct linear baroclinic response into an equivalent barotropic height tendency [*Hoskins and Karoly*, 1981; *Hendon and Hartmann*, 1982; *Peng and Whitaker*, 1999; *Peng et al.*, 2003]. To quantify the role of synoptic eddy vorticity flux, the vertically integrated height tendency (Z_t) due to vorticity flux convergence by synoptic transient eddies is calculated from a quasi-geostrophic potential vorticity equation [e.g., *Lau and Nath*, 1990; *Nakamura et al.*, 1997], i.e.,

$$Z_t = (f/g)\nabla^{-2}\left[-\nabla\left(\overline{v'\zeta'}\right)\right],$$

where the subscript denotes the partial derivative, the primes represent the synoptic fields, and the overbar indicates the winter mean. Z, v, and ζ denote the geopotential height, meridional wind, and relative vorticity,
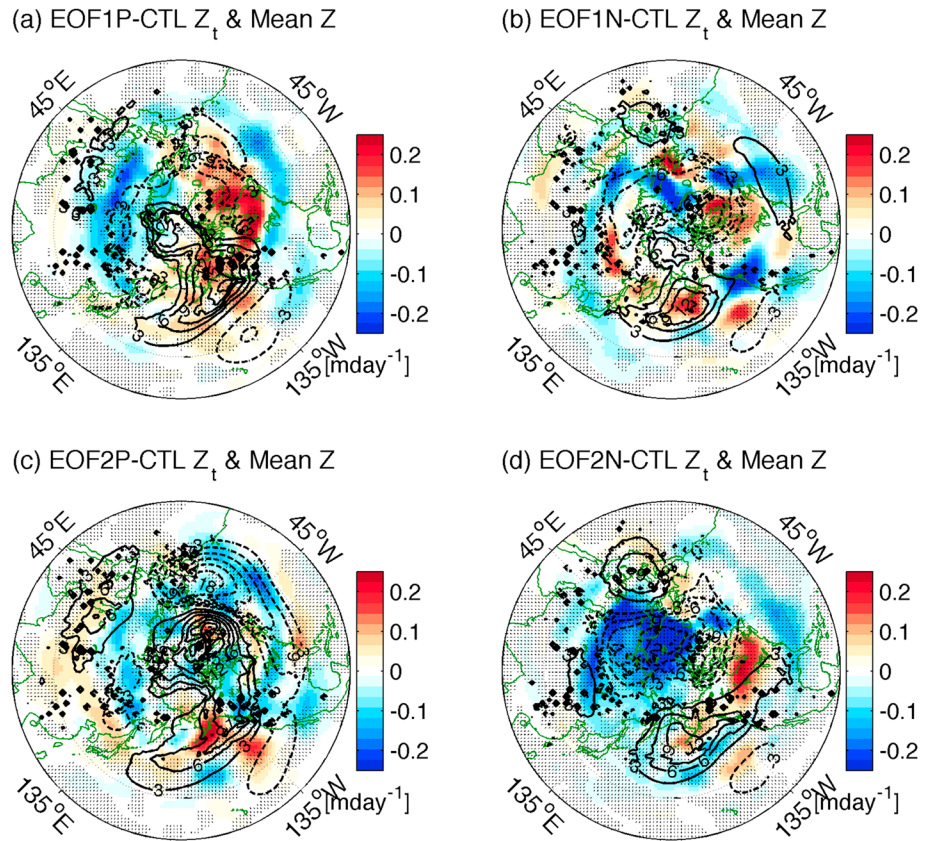
Figure 21. (a–d) Equilibrium response (NDJFMA mean excluding first 15 days) in vertically integrated (1000 hPa to 100 hPa) tendency of the geopotential height (Z_t, [m day^{-1}]) induced by the convergence of eddy vorticity flux due to synoptic baroclinic eddies (shading, [m day^{-1}]), which is overlaid with the response of the vertically integrated geopotential height (contours, [m], CI = 3 m). Positive (negative) height responses are denoted as solid (dashed) contours. Dots denote the areas of significant ($p = 0.05$) change in Z_t.

respectively. The RHS is calculated first at the individual levels and then vertically integrated between 1000 hPa and 100 hPa to form a barotropic geopotential height tendency, Z_t (LHS). In solving the Poisson equation, we suppose Z_t satisfies the simple Dirichlet boundary condition so that $Z_t = 0$ at the southern edge of the domain d01 (Figure 2), a reasonable assumption in that synoptic eddy activity is small in the tropics [*Nakamura et al.*, 1997]. The extent to which the response in height tendency by synoptic eddies is collocated with that of low-frequency circulation anomaly would then imply the positive impact of the former on the latter [e.g., *Hoskins et al.*, 1983; *Lau and Holopainen*, 1984; *Palmer and Sun*, 1985; *Lau and Nath*, 1990; *Taguchi et al.*, 2012].

Figure 21 shows the equilibrium response in Z_t (shading) superposed onto that of vertically integrated seasonal mean geopotential height (contours) representing the time-mean flow responses. In all four cases, it is clear that there is a good spatial correspondence between the enhanced Z_t (reddish shading) and the positive time-mean flow response (black solid contours) in the Gulf of Alaska. This is strong evidence that synoptic eddies play a critical role in reinforcing, via eddy vorticity convergence, the quasi-stationary anticyclonic anomalies in the downstream. The demonstrated role of altered synoptic eddy forcing in the low-frequency circulation in the North Pacific is in line with the studies [e.g., *Hall et al.*, 2001; *Walter et al.*, 2001; *Kushnir et al.*, 2002; *Wang et al.*, 2013] showing that the diabatic heating over the northwest Pacific positively feeds back via synoptic transient eddies to form a downstream equivalent barotropic ridge. Our study suggests that this is also the case with the relatively small extent and moderate amplitude SST anomalies in the EJS. Despite the lack of strong initial baroclinic (symmetric) response in height fields (Figure 12), the small-amplitude diabatic forcing in the EJS effectively trigger nonlinear low-frequency height responses via transient eddy feedback. This implies the potentially important role of the EJS, and potentially other East Asian marginal seas, in the remote atmospheric circulation system.

7. Conclusion and Discussion

The purpose of this study is to investigate, using a numerical model, the local and remote, and transient and quasi-steady response in the Northern Hemisphere atmosphere to the winter SST variability in the semi-enclosed EJS. The scale interaction between a marginal sea and the circumglobal atmospheric circulation is represented by a hemispheric regional atmospheric model with two-way multiple nesting, permitting both a downscaling and upscaling effect. With large ensembles and extended-period simulations, some verisimilitude of the model solution to the nature and some improved statistical robustness of the response are achieved in this study. Climatological conditions lacking influence from the tropical SST variability are imposed at the model's boundaries to aid in the straightforward detection of the midlatitude atmospheric dynamics that shape the equilibrium response of our interest.

Four perturbation experiments forced with dominant modes of SST variability in the EJS are compared to otherwise identical CTL simulation, driven by the climatological lateral and surface boundary conditions. EOF analysis of the NDJFMA EJS SST reveals the basin-wide warming and cooling with the peak anomaly up to ±1°C near the subpolar front as its first mode, and the northeast-southwest dipolar pattern of the peak normalized anomaly up to ±0.5°C as the second. Both the positive and negative patterns of each of the two EOF modes are used as the SST anomaly forcing to determine symmetricity of the responses to polarity and amplitude of the SST anomalies.

The local near-surface atmospheric conditions that are in direct contact with anomalous diabatic forcing in the EJS exhibit a symmetric and linear response with respect to the sign of the SST anomaly. This linear response is explained by two dynamical processes for the SST-wind relationship in the MABL, but on different spatial scales. In the EJS, the basin-wide increase (decrease) in wind speed, and also in precipitation, is associated with the anomalously warm (cold) basin-wide SST. This is consistent with the mechanism by *Wallace et al.* [1989] and *Hayes et al.* [1989] attributing the accelerated near-surface wind speed over warm SST to the weakened statistic stability of the MABL and the enhanced downward turbulent mixing of momentum. In this study, the effect of stability modulation is shallow and confined within the PBL, while that of the nonlinear large-scale circulation change dominates the response above the PBL and the lower troposphere. However, the apparent quadrature relationship between intrabasin SST and wind speed cannot be explained by the vertical mixing mechanism, which would produce an in-phase relationship. This suggests that a different mechanism is at work to determine the simulated phase relationship. We suggest that the SLP adjustment mechanism based on the linear mixed layer model by *Lindzen and Nigam* [1987] would better account for the quadrature relationship via the modulation of SLP and the concomitant cross-frontal flows. The quadrature phase relationship between wind speed and SST is expected with the SLP adjustment mechanism since $\nabla^2 P$ (or $\nabla^2 SST$) is what drives $\nabla \cdot \vec{u}$. The narrowness of the length scale in wind speed response is related to the requirement of the ∇^2 operator, which would more effectively emphasize the small-scale features such as the SST front [e.g., *Seo and Yang*, 2013; *Lambaerts et al.*, 2013]. This is consistent with a recent study [*Liu et al.*, 2013] suggesting that the scalar wind speed response is more pronounced over the warm flank of the East China Sea Kuroshio SST front, which they attributed to the vertical mixing mechanism, while the vector wind response peaks across the front (hence a narrower length scale), which is associated with the SLP adjustment mechanism. They further suggest that these two mechanisms are manifested more strongly in different timescales, with the former in the long-term mean and the latter at synoptic timescales, respectively. The clearer wind and precipitation response in the southern EJS basin in this study is related to the greater fetch that the EJS basin provides in the south, which facilitates the anomalous flows to intensify there. This implies a strong sensitivity of the local atmosphere to the SST anomalies in the southern portion of the EJS.

This linear and symmetric response in the local near-surface atmospheric conditions suggests the critical role of the intrabasin structure of the SST anomalies on the simulation and prediction of the wintertime regional atmospheric conditions. Figure 5, for example, suggests that when the EJS SST anomaly is dominated by the first EOF pattern, the central to the northern portion of the Honshu Island receives the most amount of the anomalous precipitation. When the EOF2-type SST anomaly is dominant, in contrast, the precipitation anomalies occur largely over the open water with little impact on the Honshu Island.

It is also demonstrated that the EJS SST anomalies have a far-reaching impact on the large-scale atmospheric circulation over the North Pacific. The evolution of the geopotential height response beyond the EJS for the initial 5 days is weakly baroclinic, which is rapidly replaced with an equivalent barotropic structure with a

hemispheric spatial extent and greater amplitude than the initial one. In all four SST perturbation experiments, an equivalent barotropic ridge pattern emerges as the common response in the Gulf of Alaska. The spatial pattern in height response is predominantly antisymmetric, which bears a close resemblance to the second EOF mode of the Northern Hemisphere SLP, representing the Aleutian Low mode. These anomalous ridges have dominantly intraseasonal (8–90 days) timescales, suggesting that they have characteristics similar to the blocking anticyclones.

The blocking response in the Gulf of Alaska is accompanied by the increased synoptic transient eddy variability in the northwest Pacific, which is associated with the increased baroclinicity in the EJS. As a result of intensified synoptic eddy activity, the main storm track region in the KOE experiences increased air temperature, reduced near-surface baroclinicity, and decreased Eady growth rate. This change is primarily a dynamical consequence of the increased storm track variability, which overcomes the thermal damping effect by the anomalous upward surface turbulent heat flux. In earlier studies where the surface diabatic forcing is applied to the oceanic frontal zones and main storm track regions [e.g., *Minobe* et al., 2008; *Taguchi et al.*, 2009; *Small et al.*, 2013], such measures of the near-surface baroclinicity as $dT2/dy$ or Eady growth rate would represent the environmental conditions that cause the storm track response. As the surface forcing is limited to only the EJS in our study, these measures of baroclinicity would thus require the opposite interpretation, such that increased storm track activity arising from the upstream conditions in the EJS causes the near-surface baroclinicity to decrease in the main storm track region as a result of meridional heat transport by synoptic transient eddies.

The temporal evolution of the response in synoptic transient baroclinic wave activity and intraseasonal circulation anomalies composited according to the evolution of this blocking anticyclone [e.g., *Nakamura and Wallace*, 1990] consistently reveals the intensified transient baroclinic wave activity prior to the emerging block in the Gulf of Alaska. The spatial correspondence of the low-frequency circulation anomalies to the height tendency due to the synoptic eddy vorticity flux convergence confirms this causality, suggesting the critical role of the enhanced upstream synoptic transient eddy in driving the downstream low-frequency circulation anomalies.

The mechanisms governing the common remote circulation response are consistent with the findings from the previous studies on the role of extratropical SST anomalies in the winter atmospheric circulations (see review by *Kushnir et al.* [2002]). Despite the much smaller spatial extent of anomalous surface boundary forcing than those that have been considered in previous studies, a significant large-amplitude response pattern emerges in the downstream circulation. This appears to be closely related to the fact that EJS is located in the vicinity of the North Pacific storm track, such that small perturbation in SST can effectively trigger a significant response in storm track variability. The similarity in equilibrium downstream response independent of the properties of the diabatic forcing implies that the detailed pattern of the EJS SST anomalies is perhaps not critical for the downstream anomalous ridge response. Furthermore, the nonlinear response is excited with the spatial pattern and timescales closely tied to the internal atmospheric variability found in the control experiment.

This study considers only the equilibrium response for the entire winter (NDJFMA) period. However, the midlatitude atmospheric response to the same extratropical SST anomalies undergoes a significant subseasonal variation in association with the evolution of the background state and teleconnections triggering different storm track response [e.g., *Peng et al.*, 1995, 1997; *Kushnir et al.*, 2002; *Taguchi et al.*, 2012]. Figure 22 demonstrates this subseasonal evolution of the response by averaging Z500 response for the three different subperiods of November–December (ND, top), January–February (JF, middle), and March–April (MA, bottom). This, in comparison to the NDJFMA mean response in Figure 11, suggests that the total NDJFMA equilibrium response in each case is determined by the different phases of the subseasonal evolution. The NDJFMA mean ridge response in the Gulf of Alaska in EOF1P-CTL (Figures 22a–22c), for instance, is largely due to the response in JF (and MA to a lesser extent), while that in EOF2P-CTL (Figures 22d–22f) is explained by the responses in ND and JF. This distinctive subseasonal evolution with different types of SST anomalies motivates further numerical experiments starting in different months in the winter, e.g., before/during/after the midwinter suppression of baroclinic wave activity in the Pacific [*Nakamura*, 1992]. This will help to assess the impact of the subseasonal evolution on the equilibrium response to different types of SST anomalies. This is a topic for future research.

The demonstrated sensitivity of the local and remote atmospheric circulation to the SST anomalies in the East Asian marginal seas motivates further studies on the processes leading to the SST anomalies in these seas.
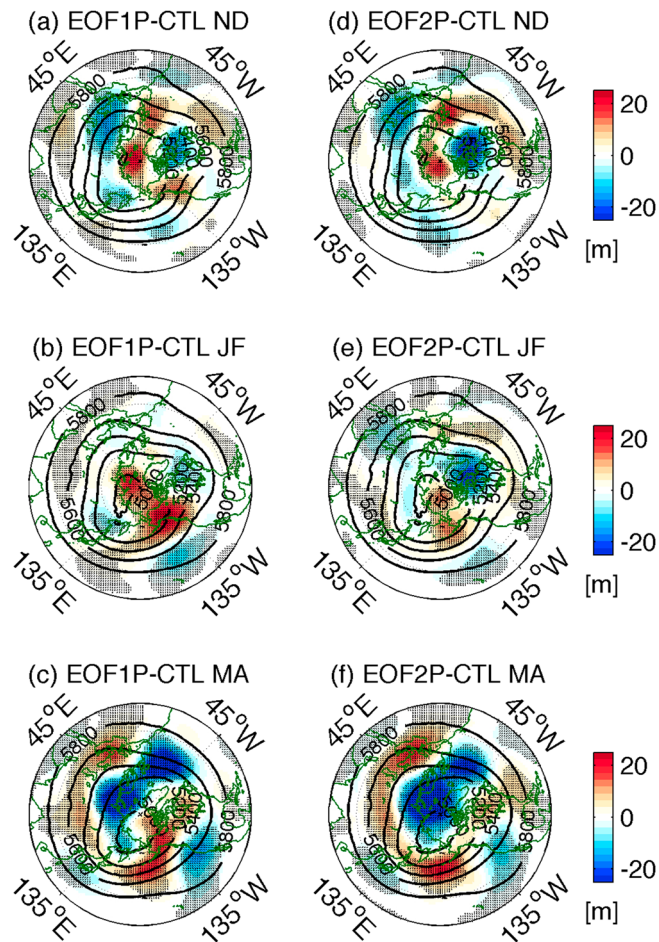
Figure 22. Response in 500 hPa geopotential height (Z500, [m], shading) averaged for (a, d) November and December (ND) only, (b, e) January and February (JF) only, (c, f) March and April (MA) only for EOF1P-CTL and EOF2P-CTL. The black contours represent the mean CTL Z500 (CI = 200 m) averaged for the corresponding periods. Dots denote the areas of significant ($p = 0.05$) response in Z500.

The representation of the oceanic variability and air-sea interaction process within these marginal seas, underrepresented in the contemporary climate models, may have far-reaching impact on the potential predictability of the extratropical atmospheric general circulation. *Hirose et al.* [2009] suggested that the autumn volume transport variability of the Tsushima Warm Current (TWC) is highly correlated with the winter SSTs in the southern portion of the EJS, to which, as our result suggests, the response in the local atmosphere and the downstream storm track variability is particularly sensitive. The fact that the variability of TWC could be associated with the changes in the Kuroshio Extension [e.g., *Ma et al.*, 2010] and East China Sea Kuroshio [e.g., *Ichikawa and Beardsley*, 2002], and also the large-scale atmospheric circulation, suggests a possible multiscale two-way coupling between the oceanic and atmospheric circulation in the North Pacific involving its marginal seas. As the ocean-to-atmosphere feedback in the Kuroshio-Oyashio Extension (KOE) is often emphasized as a key component for the decadal variability in the North Pacific [e.g., *Kwon et al.*, 2010], the impact of the marginal sea process on the downstream KOE ocean-atmosphere interaction should be further clarified. The current study uses the prescribed SST patterns in the atmospheric modeling framework, which cannot fully address this issue. Further modeling study is needed based on a high-resolution regional ocean-atmosphere model [e.g., *Seo et al.*, 2007; *Iwasaki et al.*, 2014] in order to improve our understanding of air-sea interactions in the extratropics and the low-frequency climate variability involving the East Asian marginal seas. A more detailed examination of the dominant paths for winter storms and the air mass modification along their trajectory over the various parts of the East Asian marginal seas may also shed further light on their impact on the KOE ocean-atmosphere interaction and its role in the coupled atmosphere-ocean mode of decadal variability.

References

Blackmon, M. L., S. L. Mullen, and G. T. Bates (1986), The climatology of blocking events in a perpetual January simulation of a spectral general circulation model, *J. Atmos. Sci.*, *43*, 1379–1405.

Cassou, C., C. Deser, and M. A. Alexander (2007), Investigating the impact of reemerging sea surface temperature anomalies on the winter atmospheric circulation over the North Atlantic, *J. Clim.*, *20*, 3510–3526.

Chelton, D. B., M. G. Schlax, M. H. Freilich, and R. F. Milliff (2004), Satellite measurements reveal persistent small-scale features in ocean winds, *Science*, *303*, 978–983.

Chelton, D. B., S. K. Esbensen, M. G. Schlax, N. Thum, M. H. Freilich, F. J. Wentz, C. L. Gentemann, M. J. McPhaden, and P. S. Schopf (2001), Observations of coupling between surface wind stress and sea surface temperature in the eastern tropical Pacific, *J. Clim.*, *14*, 1479–1498.

Chen, S. S., W. Zhao, J. E. Tenerelli, R. H. Evans, and V. Halliwell (2001), Impact of the AVHRR sea surface temperature on atmospheric forcing in the Japan/East Sea, *Geophys. Res. Lett.*, *28*(24), 4539–4542.

Chu, C., X.-Q. Yang, X. Ren, and T. Zhou (2013), Response of Northern Hemisphere storm tracks to Indian-western Pacific Ocean warming in atmospheric general circulation models, *Clim. Dyn.*, *40*, 1057–1070.

Deser, C., G. Magnusdottir, R. Saravanan, and A. Phillips (2004), The effects of North Atlantic SST and sea-ice anomalies on the winter circulation in CCM3, Part II: Direct and indirect components of the response, *J. Clim.*, *17*, 877–889.

Deser, C., R. A. Tomas, and S. Peng (2007), The transient atmospheric circulation response to North Atlantic SST and sea ice anomalies, *J. Clim.*, *20*, 4751–4767.

Dole, R. M. (1986), *The Life Cycles of Persistent Anomalies and Blocking Over the North Pacific*, Advances in Geophysics, vol. 29, pp. 31–69, Academic Press, Orlando.

Dole, R. M. (1989), Life cycles of persistent anomalies. Part I: Evolution of 500 mb height fields, *Mon. Weather Rev.*, *117*, 177–221.

Dorman, C. E., R. C. Beardsley, N. A. Dashko, C. A. Friehe, D. Khelif, K. Cho, R. Limeburner, and S. Varlamov (2004), Winter atmospheric conditions over the Japan Sea, *J. Geophys. Res.*, *109*, C12011, doi:10.1029/2001JC001197.

Drévillon, M., C. Cassou, and L. Terray (2003), Model study of the North Atlantic regional atmospheric response to autumn tropical Atlantic sea-surface-temperature anomalies, *Q. J. R. Meteorol. Soc.*, *129*, 2591–2611.

Iwasaki, S., A. Isobe, and S. Kako (2014), Atmosphere—Ocean Coupled Process Along Coastal Areas of the Yellow and East China Seas in Winter, *J. Clim.*, *27*, 155–167, doi:10.1175/JCLI-D-13-00117.1.

Ferranti, L., F. Molteni, and T. N. Palmer (1994), Impact of localized tropical and extratropical SST anomalies in ensembles of seasonal GCM integrations, *Q. J. R. Meteorol. Soc.*, *120*, 1613–1645.

Ferreira, D., and C. Frankignoul (2005), The transient atmospheric response to midlatitude SST anomalies, *J. Clim.*, *18*, 1049–1067.

Ferreira, D., and C. Frankignoul (2008), Transient atmospheric response to interactive SST anomalies, *J. Clim.*, *21*, 584–592.

Frankignoul, C. (1985), Sea surface temperature anomalies, planetary waves and air-sea feedback in the middle latitudes, *Rev. Geophys.*, *23*, 357–390.

Frankignoul, C., and K. Hasselmann (1977), Stochastic climate models. 2. Application to sea-surface temperature anomalies and thermocline variability, *Tellus*, *29*, 289–305.

Frankignoul, C., and R. W. Reynolds (1983), Testing a dynamical model for midlatitude sea surface temperature anomalies, *J. Phys. Oceanogr.*, *13*, 1131–1145.

Frankignoul, C., and N. Sennéchael (2007), Observed influence of North Pacific SST anomalies on the atmospheric circulation, *J. Clim.*, *20*, 592–606.

Frankignoul, C., N. Sennéchael, Y.-O. Kwon, and M. A. Alexander (2011), Influence of the meridional shifts of the Kuroshio and the Oyashio extensions on the atmospheric circulation, *J. Clim.*, *24*, 762–777.

Haines, K., and J. Marshall (1987), Eddy-forced coherent structures as a prototype of atmospheric blocking, *Q. J. R. Meteorol. Soc.*, *113*, 681–709.

Hall, N. M. J., J. Derome, and H. Lin (2001), The extratropical signal generated by a midlatitude SST anomaly. Part I: Sensitivity at equilibrium, *J. Clim.*, *14*, 2035–2053.

Hayes, S. P., M. J. McPhaden, and J. M. Wallace (1989), The influence of sea surface temperature on surface wind in the eastern equatorial Pacific: Weekly to monthly variability, *J. Clim.*, *2*, 1500–1506.

Hendon, H. H., and D. L. Hartmann (1982), Stationary waves on a sphere: Sensitivity to thermal feedback, *J. Atmos. Sci.*, *39*, 1906–1920.

Hirose, N., and K. Fukudome (2006), Monitoring the Tsushima warm current improves seasonal prediction of the regional snowfall, *Sci. Online Lett. Atmos.*, *2*, 061–063.

Hirose, N., K. Nishimura, and M. Yamamoto (2009), Observational evidence of a warm ocean current preceding a winter teleconnection pattern in the northwestern Pacific, *Geophys. Res. Lett.*, *36*, L09705, doi:10.1029/2009GL037448.

Horel, J. D., and J. M. Wallace (1981), Planetary-scale atmospheric phenomena associated with the Southern Oscillation, *Mon. Weather Rev.*, *109*, 813–829.

Hoskins, B. J., and D. J. Karoly (1981), The steady linear response of a spherical atmosphere to thermal and orographic forcing, *J. Atmos. Sci.*, *38*, 1179–1196.

Hoskins, B. J., and P. J. Valdes (1990), On the existence of storm-tracks, *J. Atmos. Sci.*, *47*, 1854–1864.

Hoskins, B. J., I. N. James, and G. H. White (1983), The shape, propagation, and mean-flow interaction of large-scale weather systems, *J. Atmos. Sci.*, *40*, 1595–1612.

Ichikawa, H., and R. C. Beardsley (2002), The current system in the Yellow Sea and East China Sea, *J. Oceanogr.*, *58*, 77–92, doi:10.1023/A:1015876701363.

Isobe, A., and R. C. Beardsley (2007), Atmosphere and marginal-sea interaction leading to an interannual variation in cold-air outbreak activity over the Japan Sea, *J. Clim.*, *20*, 5707–5714.

Kalnay, E., et al. (1996), The NCEP/NCAR 40-year reanalysis project, *Bull. Am. Meteorol. Soc.*, *77*, 437–471.

Kelly, K. A., R. J. Small, R. M. Samelson, B. Qiu, T. M. Joyce, M. Cronin, and Y.-O. Kwon (2010), Western boundary currents and frontal air-sea interaction: Gulf Stream and Kuroshio Extension, *J. Clim.*, *23*, 5644–5667.

Keshavamurty, R. N. (1982), Response of the atmosphere to sea surface temperature anomalies over the equatorial Pacific and the teleconnections of the Southern Oscillation, *J. Atmos. Sci.*, *39*, 1241–1259.

Kushnir, Y., and N. C. Lau (1992), The general circulation model response to a North Pacific SST anomaly: Dependence on timescale and pattern polarity, *J. Clim.*, *5*, 271–283.

Kushnir, Y., W. A. Robinson, I. Blade, N. M. J. Hall, S. Peng, and R. Sutton (2002), Atmospheric GCM response to extratropical SST anomalies: Synthesis and evaluation, *J. Clim.*, *15*, 2233–2256.

Kwon, Y.-O., M. A. Alexander, N. A. Bond, C. Frankignoul, H. Nakamura, B. Qiu, and L. A. Thompson (2010), Role of the Gulf Stream and Kuroshio-Oyashio systems in large-scale atmosphere-ocean interaction: A review, *J. Clim.*, *23*, 3249–3281.

Kwon, Y.-O., C. Deser, and C. Cassou (2011), Coupled atmosphere-mixed layer ocean response to ocean heat flux convergence along the Kuroshio Current Extension, *Clim. Dyn.*, *36*, 2295–2312.

Lambaerts, J., G. Lapeyre, R. Plougonven, and P. Klein (2013), Atmospheric response to sea surface temperature mesoscale structures, *J. Geophys. Res. Atmosphres*, *118*, 9611–9621, doi:10.1002/jgrd.50769.

Latif, M., and T. P. Barnett (1994), Causes of decadal climate variability over the North Pacific and North America, *Science*, *266*, 634–637.

Latif, M., and T. P. Barnett (1996), Decadal climate variability over the North Pacific and North America: Dynamics and predictability, *J. Clim.*, *9*, 2407–2423.

Lau, N.-C., and E. O. Holopainen (1984), Transient eddy forcing of the time-mean flow as identified by geopotential tendencies, *J. Atmos. Sci.*, *41*, 313–328.

Lau, N.-C., and M. J. Nath (1990), A general circulation model study of the atmospheric response to extratropical SST anomalies observed in 1950–79, *J. Clim.*, *3*, 965–989.

Li, Z. X., and S. Conil (2003), Transient response of an atmospheric GCM to North Atlantic SST anomalies, *J. Clim.*, *16*, 3993–3998.

Li, S., W. A. Robinson, M. P. Hoerling, and K. M. Weickmann (2007), Dynamics of the extratropical response to a tropical Atlantic SST anomaly, *J. Clim.*, *20*, 560–574.

Lindzen, R. S., and S. Nigam (1987), On the role of sea surface temperature gradients in forcing low-level winds and convergence in the tropics, *J. Atmos. Sci.*, *44*, 2418–2436.

Liu, Z., and L. Wu (2004), Atmospheric response to North Pacific SST anomaly: The role of ocean-atmosphere coupling, *J. Clim.*, *17*, 1859–1882.

Liu, J.-W., S.-P. Zhang, and S.-P. Xie (2013), Two types of surface wind response to the East China Sea Kuroshio Front, *J. Clim.*, *26*, 8616–8627.

Ma, C., J. Yang, D. Wu, and X. Lin (2010), The Kuroshio Extension: A leading mechanism for the seasonal sea-level variability along the west coast of Japan, *Ocean Dyn.*, *60*, 667–672.

Magnusdottir, G., C. Deser, and R. Saravanan (2004), The effects of North Atlantic SST and sea-ice anomalies on the winter circulation in CCM3. Part I: Main features and storm-track characteristics of the response, *J. Clim.*, *17*, 857–876.

Manabe, S. (1957), On the modification of air mass over Japan Sea when the outburst of cold air predominates, *J. Meteorol. Soc. Jpn.*, *35*, 311–326.

Minato, S., and R. Kimura (1980), Volume transport of the western boundary current penetrating into a marginal sea, *J. Oceanogr. Soc. Jpn.*, *36*, 185–195.

Minobe, S., A. Sako, and M. Nakamura (2004), Interannual to interdecadal variability in the Japan Sea based on a new gridded upper water temperature dataset, *J. Phys. Oceanogr.*, *34*, 2382–2397, doi:10.1175/JPO2627.1.

Minobe, S., A. Kuwano-Yoshida, N. Komori, S.-P. Xie, and R. J. Small (2008), Influence of the Gulf Stream on the troposphere, *Nature*, *452*, 206–209.

Na, J.-Y., J.-W. Seo, and H.-J. Lie (1999), Annual and seasonal variations of the sea surface heat fluxes in the East Asian marginal seas, *J. Oceanogr.*, *55*, 257–270.

Na, H., K.-Y. Kim, K.-I. Chang, J. J. Park, K. Kim, and S. Minobe (2012), Decadal variability of the upper ocean heat content in the East/Japan Sea and its possible relationship to northwestern Pacific variability, *J. Geophys. Res.*, *117*, C02017, doi:10.1029/2011JC007369.

Nakamura, H. (1992), Midwinter suppression of baroclinic wave activity in the Pacific, *J. Atmos. Sci.*, *49*, 1629–1642.

Nakamura, H., and J. M. Wallace (1990), Observed changes in baroclinic wave activity during the life cycles of low-frequency circulation anomalies, *J. Atmos. Sci.*, *47*, 1100–1116.

Nakamura, H., M. Nakamura, and J. L. Anderson (1997), The role of high- and low-frequency dynamics and blocking formation, *Mon. Weather Rev.*, *125*, 2074–2093.

Ninomiya, K. (1964), Heat budget over the Japan Sea and the Japan Islands during the period of heavy snow storm, *Pap. Meteorol. Geophys.*, *15*, 52–70.

Nonaka, M., and S.-P. Xie (2003), Covariations of sea surface temperature and wind over the Kurishio and its extension: Evidence for ocean-to-atmosphere feedback, *J. Clim.*, *16*, 1404–1413.

O'Neill, L. W., D. B. Chelton, S. K. Esbensen, and F. J. Wentz (2005), High-resolution satellite measurements of the atmospheric boundary layer response to SST variations along the Agulhas Return Current, *J. Clim.*, *18*, 2706–2723.

Palmer, T. N., and Z. Sun (1985), A modeling and observational study of the relationship between sea-surface temperature in the northwest Atlantic and the atmospheric general circulation, *Q. J. R. Meteorol. Soc.*, *111*, 947–975.

Peng, S., and W. A. Robinson (2001), Relationships between atmospheric internal variability and the responses to an extratropical SST anomaly, *J. Clim.*, *14*, 2943–2959.

Peng, S., and J. S. Whitaker (1999), Mechanisms determining the atmospheric response to midlatitude SST anomalies, *J. Clim.*, *12*, 1393–1408.

Peng, S., A. Mysak, H. Ritchie, J. Derome, and B. Dugas (1995), The difference between early and middle winter atmospheric response to sea surface temperature anomalies in the northwest Atlantic, *J. Clim.*, *8*, 137–157.

Peng, S., A. Robinson, and M. P. Hoerling (1997), The modeled atmospheric response to midlatitude SST anomalies and its dependence on background circulation states, *J. Climate*, *10*, 971–987.

Peng, S., W. A. Robinson, and S. Li (2003), Mechanisms for the NAO responses to the North Atlantic SST tripole, *J. Clim.*, *16*, 1,987–2,004.

Pitcher, E. J., M. L. Blackmon, G. T. Bates, and S. Munoz (1988), The effect of North Pacific sea surface temperature anomalies on the January climate of a general circulation model, *J. Atmos. Sci.*, *45*, 172–188.

Renwick, J. A., and J. M. Wallace (1996), Relationships between North Pacific wintertime blocking, El Niño, and the PNA pattern, *Mon. Weather Rev.*, *124*, 2071–2076.

Reynolds, R. W., T. M. Smith, C. Liu, D. B. Chelton, K. S. Casey, and M. G. Schlax (2007), Daily high-resolution-blended analyses for sea surface temperature, *J. Clim.*, *20*, 5473–5496.

Seo, H., and J. Yang (2013), Dynamical response of the Arctic atmospheric boundary layer process to uncertainties in sea ice concentration, *J. Geophys. Res. Atmospheres*, *118*, 12,383–12,402, doi:10.1002/2013JD020312.

Seo, H., A. J. Miller, and J. O. Roads (2007), The Scripps Coupled Ocean-Atmosphere Regional (SCOAR) model, with applications in the eastern Pacific sector, *J. Clim.*, *20*, 381–402.

Shimada, T., and H. Kawamura (2006), Satellite observations of sea surface temperature and sea surface wind coupling in the Japan Sea, *J. Geophys. Res.*, *111*, C08010, doi:10.1029/2005JC003345.

Shimada, T., and H. Kawamura (2008), Satellite evidence of wintertime atmospheric boundary layer responses to multiple SST fronts in the Japan Sea, *Geophys. Res. Lett.*, *35*, L23602, doi:10.1029/2008GL035810.

Shimada, T., and S. Minobe (2011), Global analysis of the pressure adjustment mechanism over sea surface temperature fronts using AIRS/Aqua data, *Geophys. Res. Lett.*, *38*, L06704, doi:10.1029/2010GL046625..

Shutts, G. J. (1983), The propagation of eddies in diffluent jetstreams: Eddy vorticity forcing of blocking flow fields, *Q. J. R. Meteorol. Soc.*, *109*, 737–761.

Skamarock, W. C., J. B. Klemp, J. Dudhia, D. O. Gill, D. M. Barker, M. G. Duda, X.-Y. Huang, W. Wang, and J. G. Powers (2008), A description of the advanced research WRF version 3.NCARTech, Note NCAR/TN-4751STR, 113 pp.

Small, R. J., S.-P. Xie, and Y. Wang (2003), Numerical simulation of atmospheric response to pacific tropical instability waves, *J. Climate*, *16*, 3723–3741.

Small, R. J., S. de Szoeke, S. P. Xie, L. O'Neill, H. Seo, Q. Song, P. Cornillon, M. Spall, and S. Minobe (2008), Air-sea interaction over ocean fronts and eddies, *Dyn. Ocean Atmos.*, *45*, 274–319.

Small, R. J., R. A. Tomas, and F. O. Bryan (2013), Storm track response to ocean fronts in a global high-resolution climate model, *Clim. Dyn.*, doi:10.1007/s00382-013-1980-9.

Taguchi, B., H. Nakamura, M. Nonaka, and S.-P. Xie (2009), Influences of the Kuroshio/Oyashio Extensions on air–sea heat exchanges and storm-track activity as revealed in regional atmospheric model simulations for the 2003/04 cold season, *J. Clim.*, *22*, 6536–6560.

Taguchi, B., H. Nakamura, M. Nonaka, N. Komori, A. Kuwano-Yoshida, K. Takaya, and A. Goto (2012), Seasonal evolutions of atmospheric response to decadal SST anomalies in the North Pacific Subarctic Frontal Zone: Observations and a coupled model simulation, *J. Clim.*, *25*, 111–139.

Takahashi, H. G., N. N. Ishizaki, H. Kawase, M. Hara, T. Yoshikane, X. Ma, and F. Kimura (2013), Potential impact of sea surface temperature on winter precipitation over the Japan Sea Side of Japan: A regional climate modeling study, *J. Meteorol. Soc. Jpn.*, *91*(4), 471–488.

Takano, Y., Y. Tachibana, and K. Iwamoto (2008), Influences of large-scale atmospheric circulation and local sea surface temperature on convective activity over the Sea of Japan in December, *Sci. Online Lett. Atmos.*, *4*, 113–116.

Takatama, K., S. Minobe, M. Inatsu, S.-P. Xie, and R. Small (2012), Diagnostics for near-surface wind convergence/divergence response to the Gulf Stream in a regional atmospheric model, *Atmospheric Science Letters*, *12*, 206–209.

Thompson, D. W. J., and J. M. Wallace (1998), The Arctic Oscillation signature in the wintertime geopotential height and temperature fields, *Geophys. Res. Lett.*, *25*, 1297–1300.

Ting, M., and S. Peng (1995), Dynamics of the early and middle winter atmospheric responses to the Northwest Atlantic SST anomalies, *J. Clim.*, *8*, 2239–2254.

Wallace, J. M., and D. S. Gutzler (1981), Teleconnections in the geopotential height field during the Northern Hemisphere Winter, *Mon. Weather Rev.*, *109*, 784–812.

Wallace, J. M., T. P. Mitchell, and C. Deser (1989), The influence of sea surface temperature on surface wind in the eastern equatorial Pacific: Seasonal and interannual variability, *J. Clim.*, *2*, 1492–1499.

Walter, K., U. Luksch, and K. Fraedrich (2001), A response climatology of idealized midlatitude thermal forcing experiments with and without a storm track, *J. Clim.*, *14*, 467–484.

Wang, L., T. Li, and T. Zhou (2012), Intraseasonal SST variability and air–sea interaction over the Kuroshio Extension Region during boreal summer, *J. Clim.*, *25*, 1619–1634.

Wang, L., T. Li, T. Zhou, and X. Rong (2013), Origin of the intraseasonal variability over the North Pacific in boreal summer, *J. Clim.*, *26*, 1211–1229.

Watson, J. S., and S. J. Colucci (2002), Evaluation of ensemble predictions of blocking in the NCEP Global Spectral Model, *Mon. Weather Rev.*, *130*, 3008–3021.

Wiedenmann, J. M., A. R. Lupo, I. I. Mokhov, and E. A. Tikhonova (2002), The climatology of blocking anticyclones for the Northern and Southern Hemispheres: Block intensity as a diagnostic, *J. Clim.*, *15*, 3459–3473.

Yamamoto, M., and N. Hirose (2008), Influence of assimilated SST on regional atmospheric simulation: A case of a cold-air outbreak over the Japan Sea, *Atmos. Sci. Lett.*, *9*(1), 13–17.

Yamamoto, M., and N. Hirose (2009), Regional atmospheric simulation of monthly precipitation using high-resolution SST obtained from an ocean assimilation model: Application to the wintertime Japan Sea, *Mon. Weather Rev.*, *137*, 2164–2175.

Yamamoto, M., and N. Hirose (2010), Atmospheric simulations using OGCM-assimilation SST: Influence of the wintertime Japan Sea on monthly precipitation, terrestrial, *Atmos. Oceanic Sci.*, *21*(1), 113–122.

Yamamoto, M., and N. Hirose (2011), Possible modification of atmospheric circulation over the northwestern Pacific induced by a small semi-enclosed ocean, *Geophys. Res. Lett.*, *38*, L03804, doi:10.1029/2010GL046214.

Yeh, S.-W., Y.-G. Park, H.-S. Min, C.-H. Kim, and J.-H. Lee (2010), Analysis of characteristics in the sea surface temperature variability in the East/Japan Sea, *Prog. Oceangr.*, *85*, 213–223.